Multispectral incoherent holography based on measurement of differential wavefront curvature

September
2019

Department of Electrical Engineering and Computer Science
Graduate School of Engineering Iwate University
JAPAN

KITTIPHOT JIANWATTANANUKUL

Multispectral incoherent holography based on measurement of differential wavefront curvature

September 2019

KITTIPHOT JIANWATTANANUKUL

Multispectral incoherent holography based on measurement of differential wavefront curvature

September
2019

Department of Electrical Engineering and Computer Science
Graduate School of Engineering Iwate University
JAPAN

KITTIPHOT JIANWATTANANUKUL

Abstract

In this dissertation, a technique for multispectral incoherent holography based on measuring differential wavefront curvature is proposed. The differential wavefront curvature is measured and the principle of Fourier transform spectrometry is applied to provide a set of spectral components of three-dimensional (3D) images and continuous spectra for spatially incoherent, polychromatic objects. The mathematical formulation of the principle and the experimental results are presented. Spectral resolution and 3D imaging properties are investigated based on a four-dimensional (4D) impulse response function (IRF). The dissertation consists of the following six chapters.

In chapter 1, an overview of the dissertation is provided. The research background is introduced, the research objectives are stated, and the structure of the dissertation is presented.

In chapter 2, the theoretical background of the research is summarized. The properties of light are derived from the wave equation, including optical interference based on the superposition principle of two optical waves, optical coherence, diffraction theory, angular spectrum method and Fourier transform spectrometry.

In chapter 3, the concept of multispectral incoherent holography is presented. An interferometer similar to the Michelson interferometer with one plane mirror replaced with a concave mirror is described. This interferometer detects the differential wavefront curvature between two split wavefronts. After the volume interferogram is obtained, the spectral profile of an object can be found in a way analogous to Fourier transform spectrometry. A mathematical theory that can be used to retrieve spectrally resolved 3D images is described. The optical intensity of interferograms is first expressed in terms of a spatial correlation function of the optical field. This function represents the interference of optical fields reflected by the plane mirror or the concave mirror. For a stationary field, the spatial correlation function recorded in the volume interferogram can be expressed as the superposition integral of the cross-spectral density function, where the cross-spectral density function is defined as the cross correlation between the monochromatic components of the optical field. This cross-spectral density function can be expressed in terms of the spectral density function of the measured object and is equivalent to a spectral component of the complex incoherent hologram. Thus, the 3D image for each spectrum can be reconstructed from the complex incoherent hologram by applying conventional inverse propagation techniques.

In chapter 4, two experiments are described. In the first experiment, the measured object is polychromatic. The 3D volume interferogram is measured with the interferometer. By performing a Fourier transform of the volume interferogram with respect to thickness, the spectral profile of the object and the complex incoherent hologram for each spectral component are obtained. The 3D image at the spectral peak is reconstructed from the complex incoherent hologram. The second experiment uses two polychromatic objects. The spectral profiles of the objects are analyzed at a point on the plane perpendicular to the optical axis. The experimental results show that the shape of the measured object is reconstructed well, the size of the object is close to that of the original, and the depth distance of the object is recovered.

In chapter 5, the imaging properties of multispectral incoherent holography are investigated theoretically by deriving an analytical solution of the IRF. The derivation is performed under the paraxial approximation. To confirm the mathematical analysis, the 3D images obtained from the analytical solution of the IRF are compared with the experimental results. In the mathematical analysis, the measured object is assumed to be a monochromatic point source. The cross-spectral density function is expressed as a Fourier transform of the product of the spatial correlation function and the window function, the latter of which represents the spatial extension of the image detector. To find the IRF and reconstruct the 3D image, the inverse propagation formula is applied to the cross-spectral density function. Consequently, the final expression for the reconstructed image appears as the superposition integral of the input spectral density function and the IRF, with the IRF expressed in terms of the Fresnel integrals.

For comparison, the image is reconstructed as the IRF prediction. Another experiment is performed, in which the measured object is a monochromatic point source and the corresponding image is reconstructed. The two images are compared. The analytical solution of the IRF and the experimental results agree well, validating the method. The images obtained demonstrate the performance of the method.

The conclusions are provided in chapter 6.

Contents

I Introduction

1.1 Research background

Incoherent holography is a measurement technique that uses light. The amplitude and phase information of light waves from an object is measured according to the incoherence of the light. In contrast to a photograph, the distance to the object is recorded in an incoherent hologram. Incoherent holography is based on diffraction theory and the self-interference principle, in which light originating from each point on the object interferes with itself.

The conventional method of interferometric spectral imaging for three-dimensional (3D) objects illuminated with a natural light source[1)] was followed by the development of the synthetic aperture technique for digital holographic 3D imaging spectrometry.[2,3)] This method is also called the spherical-type method because the fringe patterns recorded in the volume interferogram are arranged in the same way as spherical wavefronts propagating from the object. Variations of the method have been developed, including the hyperbolic-type method (H-type)[4)] and the rotated hyperbolic-type method[5)]. The method has also been extended to single-pixel imaging, in which an H-type volume interferogram can be measured directly without using a synthetic aperture.[6)] Each variation has its own advantages; however, all these methods generally have a long measurement time.

In this dissertation, a method is proposed called multispectral incoherent holography, which requires a simple system and a short measurement time compared with previous methods, and thus is better suited for unstable objects, such as biological samples. A set of spectral components of the 3D images and continuous spectra for spatially incoherent polychromatic objects are obtained from the volume interferogram. Because the method is based on measuring differential wavefront curvature, it is a generalization of Fresnel incoherent correlation holography[7)] combined with Fourier transform spectrometry.

1.2 Objectives of the research

Interferometric 3D spectral imaging is performed using a two-wavefront folding interferometer and synthetic aperture processing. The two-wavefront folding interferometer obtains a five-dimensional data set and a volume interferogram is generated by performing synthetic aperture processing on the data set. Then, multispectral images are generated from this volume interferogram. However, this interferometer generally has a long measurement time and the data sizes are large. Thus, the objective of this research is to resolve these problems by measuring differential wavefront curvature. The method is validated by comparing the experimental results and the analytical solution of the impulse response function (IRF).

1.3 Structure of this dissertation

This dissertation has six chapters. Chapter 1 provides a research overview and describes the research objectives. Chapter 2 contains the related theory of the properties of optical waves, the principle of interference, the interference of two optical waves, the propagation of optical waves, Fourier transform spectrometry, the reconstruction of spectrally resolved 3D images, and signal processing methods. The theory is included to demonstrate that the properties of light can be expressed mathematically in terms of the wave equation. Thus, the properties of the interference and propagation of optical waves are discussed based on the interference principle and the diffraction phenomena. In addition, the methods of image reconstruction are based on the angular spectrum method.

Chapter 3 describes a demonstration of the proposed method. A 3D volume interferogram is obtained from an interferometer. The reconstruction process for multispectral components of 3D images based on the generalized Wiener–Khinchin theorem is presented. Chapter 4 shows the experimental conditions, interferometric measurements, and experimental results.

Chapter 5 presents a theoretical investigation of the 3D imaging properties of incoherent holography using a new analytical solution of the IRF defined over four-dimensional (4D) space. The primary result obtained in the chapter explains the full derivation of the 4D IRF, which is expressed mathematically in closed form. The theoretical predictions obtained from the analytical solution of the IRF are also shown for comparison with the experimental results. Chapter 6 gives the conclusions based on the results.

II Basis concepts of optical wave

2.1 Introduction

For coherent holography, the interference pattern of two coherence waves, namely, the object wave and the reference wave, are captured on a recording medium. Subsequently, the image is reconstructed by illuminating the hologram with coherent light. In digital incoherent holography, the hologram is constructed from incoherent waves and an optical sensor is used to record the information and a mathematical method is used to reconstruct the image.

First, a brief summary of the mathematical description of optical waves is given. Then, the interference of the optical waves that correspond to produce the hologram is explained. The reconstruction of the image is discussed in the overview of the mathematical method. The chapter is then summarized.

2.2 Mathematical description of optical waves

An electromagnetic field is described by two related vector fields: the electric field $\boldsymbol{E}(\boldsymbol{r}, t)$ and the magnetic field $\boldsymbol{B}(\boldsymbol{r}, t)$. Both are vector functions of position and time. In general, six scalar functions of position and time are therefore required to describe light in free space. Fortunately, these functions are related since they must satisfy a set of coupled paratial differential equations known as Maxwell's equations.

The electric and magnetic fields in free space satisfy the following partial differential equation, known as Maxwell's equations:

$$\mathrm{rot}\,\boldsymbol{E}(\boldsymbol{r}, t) + \frac{\partial \boldsymbol{B}(\boldsymbol{r}, t)}{\partial t} = 0, \tag{2.1}$$

$$\mathrm{rot}\,\boldsymbol{B}(\boldsymbol{r}, t) - \mu_0 \varepsilon_0 \frac{\partial \boldsymbol{E}(\boldsymbol{r}, t)}{\partial t} = 0, \tag{2.2}$$

$$\mathrm{div}\,\boldsymbol{E}(\boldsymbol{r}, t) = 0, \tag{2.3}$$

$$\mathrm{div}\,\boldsymbol{B}(\boldsymbol{r}, t) = 0, \tag{2.4}$$

where $\boldsymbol{r}$ is a vector position in space and t is time. The constants $\varepsilon_0 \approx (1/36\pi) \times 10^{-9}$ and

$\mu_0 \approx 4\pi \times 10^{-7}$ (MKS units) are, respectively, the electric permittivity and the magnetic permeability of free space; and div and rot are the divergence and the curl operations. In a Cartesian coordinate system $\mathrm{div}\boldsymbol{E}(\boldsymbol{r}, t) = \partial E_x(\boldsymbol{r}, t)/\partial x + \partial E_y(\boldsymbol{r}, t)/\partial y + \partial E_z(\boldsymbol{r}, t)/\partial z$ and $\mathrm{rot}\boldsymbol{E}(\boldsymbol{r}, t)$ is a vector with Cartesian components $(\partial E_z(\boldsymbol{r}, t)/\partial y - \partial E_y(\boldsymbol{r}, t)/\partial z,$ $\partial E_x(\boldsymbol{r}, t)/\partial z - \partial E_z(\boldsymbol{r}, t)/\partial x,\ \partial E_y(\boldsymbol{r}, t)/\partial x - \partial E_x(\boldsymbol{r}, t)/\partial y)$.

A necessary condition for $\boldsymbol{E}(\boldsymbol{r}, t)$ and $\boldsymbol{B}(\boldsymbol{r}, t)$ to satisfy Maxwell's equations is that each of their components satisfy the wave equation

$$\left(\nabla^2 - \frac{n^2}{c^2}\frac{\partial^2}{\partial t^2}\right)\boldsymbol{E}(\boldsymbol{r}, t) = 0, \tag{2.5}$$

$$\left(\nabla^2 - \frac{n^2}{c^2}\frac{\partial^2}{\partial t^2}\right)\boldsymbol{B}(\boldsymbol{r}, t) = 0, \tag{2.6}$$

where, n is the index of refraction of the medium, defined by

$$n = \left(\frac{\varepsilon}{\varepsilon_0}\right)^{\frac{1}{2}}, \tag{2.7}$$

where ε is the electric permittivity in the medium, and c is the speed of light in vacuum, given by

$$c = \frac{1}{\left(\mu_0\varepsilon_0\right)^{\frac{1}{2}}} \approx 3 \times 10^8 \text{ m/s}, \tag{2.8}$$

By using these equations, the behavior of the electric field $\boldsymbol{E}(\boldsymbol{r}, t)$ and magnetic field $\boldsymbol{B}(\boldsymbol{r}, t)$ can be summarized in three dimensions as single electromagnetic waves. For scalar theory of optical field, the optical wave can be represented by a complex optical field $V(\boldsymbol{r}, t)$, which corresponds to one component of the electric field vector.

The equation of motion is given by

$$\left(\nabla^2 - \frac{n^2}{c^2}\frac{\partial^2}{\partial t^2}\right)V(\boldsymbol{r}, t) = 0, \tag{2.9}$$

Note that in free space, the index of refraction, $\boldsymbol{n}$, is unity.

For a monochromatic field, we find a solution of the wave equation of the form

$$V(\boldsymbol{r}, t) = U(\boldsymbol{r}; \omega)\exp(-i\omega t), \tag{2.10}$$

where $U(\boldsymbol{r}; \omega)$ is the complex amplitude of a monochromatic field and $\omega = ck$ is the

angular frequency. Substituting Eq. (2.10) into the wave equations in Eq. (2.9), yields the Helmholtz equation, expressed as a special case of the wave equation

$$(\nabla^2 + k^2)U(\boldsymbol{r};\omega) = 0, \tag{2.11}$$

where, k is the wavenumber given by

$$k = \frac{2\pi}{\lambda}, \tag{2.12}$$

and λ is the wavelength in the propagation medium.

If we solve the Helmholtz equation in spherical coordinate we remind that the Laplacian operator in spherical coordinate is given by

$$\begin{aligned}&(\nabla^2 + k^2)U(\boldsymbol{r};\omega)\\ &\quad= \left(\frac{1}{r}\frac{\partial^2}{\partial r^2}r + \frac{1}{r^2\sin\theta}\frac{\partial}{\partial\theta}\sin\theta\frac{\partial}{\partial\theta} + \frac{1}{r^2\sin^2\theta}\frac{\partial^2}{\partial\varphi^2} + k^2\right)U(r,\theta,\varphi;\omega),\end{aligned} \tag{2.13}$$

and we can find solution as a spherical wave

$$U(\boldsymbol{r};\omega) = U_0\frac{\exp\left(ik\,|\boldsymbol{r}-\boldsymbol{r}_0|\right)}{|\boldsymbol{r}-\boldsymbol{r}_0|}, \tag{2.14}$$

which is a wave traveling from a point source. It is important to note the difference in the argument of the exponential. In the case of a spherical wave we have a simple product kr where $r = |\boldsymbol{r}-\boldsymbol{r}_0|$ and in the case of the plane wave this a scalar product $\boldsymbol{k}\cdot\boldsymbol{r} = k_x x + k_y y + k_z z$. It originates from a source and its wavefront consist of spheres centered about the point source (Fig. 2.1). As previously due to the convention of time $\propto \exp(-i\omega t)$ the wave described with the complex amplitude presented on Eq. (2.14) travels from the source point outwardly. On the other hand a spherical wave traveling inwards (toward the point source) is described by

$$U(\boldsymbol{r};\omega) = U_0\frac{\exp\left(-ik\,|\boldsymbol{r}-\boldsymbol{r}_0|\right)}{|\boldsymbol{r}-\boldsymbol{r}_0|}, \tag{2.15}$$

the intensity of the spherical wave decays with the distance from the point source as $I(\boldsymbol{r}) = (|U_0|^2/r^2)$.

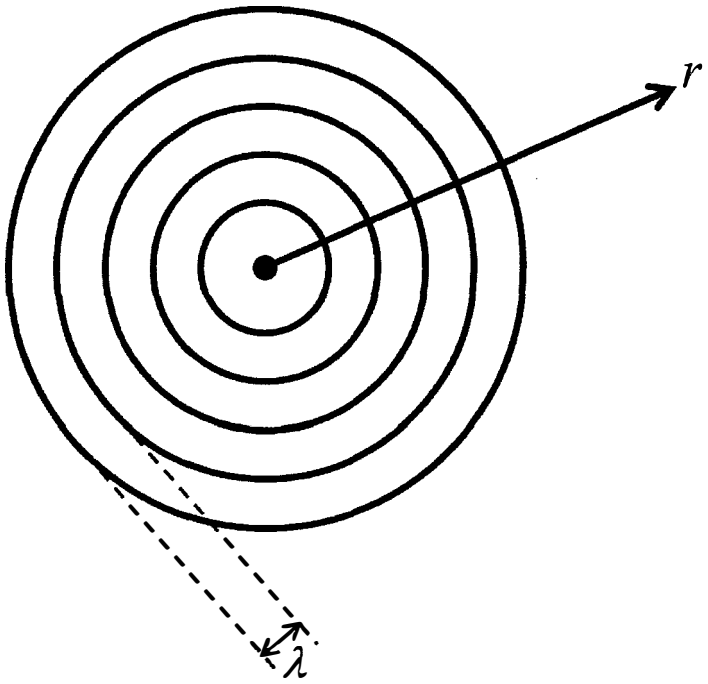

Fig. 2.1 Representation of a spherical wave.

2.3 Interference of optical waves

This section describes the interference phenomena. Among electromagnetic waves, visible light has a frequency that is too high, and there is a problem in that the wave itself cannot be detected. It is the optical intensity that can be detected, and the nature of the amplitude and phase of the optical wave can be examined from the detectable optical intensity. It is the interference effect of waves that can observe this optical wave most directly. When two optical waves are superimposed, the optical intensity changes both temporally and spatially. This is called an interference phenomenon. Measurement methods using interference phenomena are widely used and are now known as very important phenomena when dealing with light.

2.3.1 Superposition of two optical waves

When two or more optical waves overlap, an intensifying or weakening interference action occurs. If each wave is a plane wave, it is expressed as

$$V(\boldsymbol{r}, t) = a\exp\left[i\left(\boldsymbol{k}\cdot\boldsymbol{r} - \omega t + \phi\right)\right], \tag{2.16}$$

since waves with vibration directions orthogonal to each other do not interfere, the amplitude

a is represented by a scalar quantity. Here, ω is the angular frequency, t is the time, and ϕ is the initial phase.

The superposition of the two optical waves can be expressed as shown in Fig. 2.2. It is assumed that plane waves with initial phases ϕ_1 and ϕ_2 are generated from points P_1 and P_2 at position vectors $\boldsymbol{r}_1$ and $\boldsymbol{r}_2$. Here $\boldsymbol{r}-\boldsymbol{r}_1$ is the position vector up to point D starting from point P_1. Thus, $\boldsymbol{r}$ in Eq. (2.9) can be replaced by $\boldsymbol{r}-\boldsymbol{r}_1$. In this case, $\boldsymbol{k}\cdot(\boldsymbol{r}-\boldsymbol{r}_1)$ represents the phase delay when the plane wave passing through point P_1 propagates to point D.

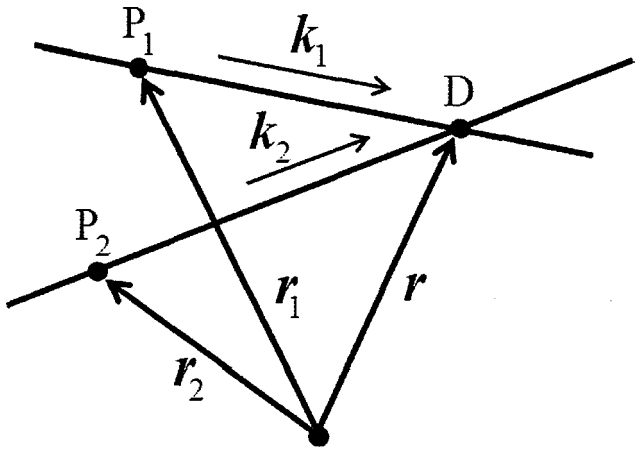

Fig. 2.2 Superposition of two light wave.

The two plane waves at observation point D and time t can be expressed as

$$V_1(\boldsymbol{r}, t) = a_1 \exp\left\{i\left[\boldsymbol{k}_1\cdot(\boldsymbol{r}-\boldsymbol{r}_1)-\omega_1 t+\phi_1\right]\right\}, \tag{2.17}$$

$$V_2(\boldsymbol{r}, t) = a_2 \exp\left\{i\left[\boldsymbol{k}_2\cdot(\boldsymbol{r}-\boldsymbol{r}_2)-\omega_2 t+\phi_2\right]\right\}, \tag{2.18}$$

the observed light intensity is

$$\begin{aligned} I(\boldsymbol{r}, t) &= \left|V(\boldsymbol{r}, t)\right|^2 \\ &= \left|V_1(\boldsymbol{r}, t)+V_2(\boldsymbol{r}, t)\right|^2 \\ &= \left|V_1(\boldsymbol{r}, t)\right|^2+\left|V_2(\boldsymbol{r}, t)\right|^2+V_1^*(\boldsymbol{r}, t)V_2(\boldsymbol{r}, t)+V_1(\boldsymbol{r}, t)V_2^*(\boldsymbol{r}, t) \\ &= I_1+I_2+2\sqrt{I_1 I_2}\cos\left[\boldsymbol{k}_2\cdot(\boldsymbol{r}-\boldsymbol{r}_2)-\boldsymbol{k}_1\cdot(\boldsymbol{r}-\boldsymbol{r}_1)-(\omega_2-\omega_1)t+(\phi_2-\phi_1)\right]. \end{aligned} \tag{2.19}$$

Here, * represents a complex conjugate, which is denoted by $I_1 = a_1^2$, $I_2 = a_2^2$. The first and second terms are the light intensity when the optical wave is present alone, and the third term is the interference term. The interference light intensity is not simply the sum of the light intensities, and becomes stronger or weaker. This phenomenon is called interference. The interference term changes with the phase difference.

2.3.2 Interference of two optical waves

Even if the optical waves from one light source are divided and made parallel to each other to be $\boldsymbol{k}_1 // \boldsymbol{k}_2$, if the frequency is slightly different and is $\omega_1 \neq \omega_2$, the interference fringes fluctuate in time. We consider the case of detecting interference fringes formed by continuous optical waves, although the frequencies are different. The two optical waves are plane waves with constant amplitude, and the angular frequency is ω_1 and ω_2. The observed interference light intensity changes temporally due to the beat phenomenon. Let the observation time be T and the average value be $\langle\ \rangle$, then

$$\langle I(\boldsymbol{r}, t)\rangle = I_1 + I_2 + \frac{2\sqrt{I_1 I_2}}{T}\int_0^T \cos\left[-(\omega_2 - \omega_1)t\right]dt. \tag{2.20}$$

If the observation time is sufficiently longer than the fluctuation period of the beat frequency, the interference term is averaged and becomes

$$\langle I(\boldsymbol{r}, t)\rangle = I_1 + I_2, \tag{2.21}$$

and no interference fringes are observed. Whether the optical waves interfere in this way depends on whether they can be observed.

Generally, visible light with two wavelengths can be separated by a spectrometer when the wavelength difference is about 0.1 nm. Suppose that two lights whose wavelengths are close come from the same direction. Let their wavelengths be $\lambda_1 = 500.0$ nm and $\lambda_2 = 500.1$ nm. If this light is expressed by frequency, it is

$$\nu = \frac{\omega}{2\pi} = \frac{c}{\lambda}, \tag{2.22}$$

so the frequency $\Delta\nu = \left(\omega_1 - \omega_2\right)/2\pi = 120$ GHz. The interference term fluctuates in time at high frequency. Considering the extreme, the observation time is assumed to be the response time of the light detector. Even if the detector responds to the speed of light up to about 10^{-9} seconds, the time-varying interference fringes are not observed because they are averaged

over 120 cycles. Generally, it is evaluated by the average intensity for a sufficiently long time. Therefore, two optical waves with different wavelengths are treated as not interfering. Therefore, it can be understood that two optical waves with different wavelengths may be treated as incoherent.

2.3.3 Mutual coherence function

Consider an interference term for optical fields that originate from two points, where the travel times from the original point to the superposed point are t_1 and t_2. The space-time correlation function, $\Gamma(\boldsymbol{r}_1, t_1, \boldsymbol{r}_2, t_2)$, of the interference is expressed as

$$\Gamma(\boldsymbol{r}_1, t_1, \boldsymbol{r}_2, t_2) = \left\langle V^*(\boldsymbol{r}_1, t_1) V(\boldsymbol{r}_2, t_2) \right\rangle. \tag{2.23}$$

At a fixed point with different paths, the longer path requires additional time $\tau = t_1 - t_2$ to traverse, and the space-time correlation function (or mutual coherence function) of these optical fields is expressed as

$$\Gamma(\boldsymbol{r}_1, \boldsymbol{r}_2, \tau) = \left\langle V^*(\boldsymbol{r}_1, t_1) V(\boldsymbol{r}_2, t_1 - \tau) \right\rangle. \tag{2.24}$$

The normalized mutual coherence function can be expressed as

$$\gamma(\boldsymbol{r}_1, \boldsymbol{r}_2, \tau) = \frac{\Gamma(\boldsymbol{r}_1, \boldsymbol{r}_2, \tau)}{\sqrt{\Gamma(\boldsymbol{r}_1, \boldsymbol{r}_1, 0)}\sqrt{\Gamma(\boldsymbol{r}_2, \boldsymbol{r}_2, 0)}}. \tag{2.25}$$

This is called the complex degree of coherence. In the case of $|\gamma(\boldsymbol{r}_1, \boldsymbol{r}_2, \tau)| = 1$, the light fields at two points in space-time are said to be coherent and have perfect correlation. Also, in the case of $|\gamma(\boldsymbol{r}_1, \boldsymbol{r}_2, \tau)| = 0$, it is said to be incoherent, and the amount of field at the two points has no correlation. Furthermore, the case of $0 < |\gamma(\boldsymbol{r}_1, \boldsymbol{r}_2, \tau)| < 1$ is said to be partially coherent. Although coherent optical waves can clearly observe interference phenomena, incoherent optical waves cannot observe interference phenomena. These two optical waves are both ideal, and many optical waves are partially coherent light. For two optical waves, when the positions are the same $(\boldsymbol{r}_1 = \boldsymbol{r}_2 = \boldsymbol{r})$ and only the time is different $(t_1 = t,\ t_2 = t + \tau)$,

$$\Gamma(\boldsymbol{r}, \tau) = \left\langle V^*(\boldsymbol{r}, t_1) V(\boldsymbol{r}, t_1 - \tau) \right\rangle \tag{2.26}$$

is obtained, and $\Gamma(\boldsymbol{r}, \tau) \equiv \Gamma(\boldsymbol{r}, \boldsymbol{r}, \tau)$ shows the temporal correlation function of the optical waves at position $\boldsymbol{r}$. This is called the temporal coherence function. This is the time domain autocorrelation function, and the inverse Fourier transform of this autocorrelation function

gives the spectral density function. In general, it is expressed as

$$S(\boldsymbol{r};\omega) = \frac{1}{2\pi}\int_{-\infty}^{\infty} \Gamma(\boldsymbol{r},\ \tau)\exp(i\omega\tau)d\tau. \tag{2.27}$$

Also, the autocorrelation function can be obtained from the spectral density function, which is expressed as

$$\Gamma(\boldsymbol{r},\ \tau) = \left\langle V^*(\boldsymbol{r},0)V(\boldsymbol{r},\tau)\right\rangle = \int_0^{\infty} S(\boldsymbol{r};\omega)\exp(-i\omega\tau)d\omega. \tag{2.28}$$

This is called the Wiener-Khinchine theorem. The mutual coherence function $\Gamma(\boldsymbol{r}_1,\ \boldsymbol{r}_2,\ \tau)$ of equation (2.24) is considered to satisfy

$$|\tau| << \frac{2\pi}{\Delta\omega} \tag{2.29}$$

if the time difference τ (coherence time) of the two light fields is sufficiently small compared to $\Delta\omega$, which is the spread of the spectral density function $S(\boldsymbol{r};\omega)$. At this time, it can be regarded as the time difference $\tau = 0$. Therefore, if the position is different $(\boldsymbol{r}_1 \neq \boldsymbol{r}_2)$ in Eq. (2.24) and the time is the same $(t_1 = t_2 = t)$, then

$$\Gamma(\boldsymbol{r}_1,\ \boldsymbol{r}_2) = \left\langle V^*(\boldsymbol{r}_1,\ t),V(\boldsymbol{r}_2,\ t)\right\rangle. \tag{2.30}$$

It represents the spatial correlation of the optical field at different locations, and is called the spatial coherence function.

2.4 Propagation of optical waves

This section describes the diffraction phenomenon. Electromagnetic waves propagate as they propagate through space. This phenomenon is called diffraction, and optical waves also have diffraction effects. Optical waves have extremely high frequency, small diffraction effects compared to radio waves, and strong directivity of propagation. Therefore, spatial distribution of amplitude and phase, that is, image information can be transmitted directly.

2.4.1 Diffraction phenomenon

An optical wave propagate in space by repetition of one wavefront serving as a light source, generating the next wavefront, and the wavefront generating the next wavefront. As shown in

Fig. 2.3, it is assumed that a spherical wave is generated at point O. The equiphase surface is spherical around the point O. It is assumed that point P is on the spherical surface and secondary wave is generated from a minute region near it. The secondary generated from a minute region is a spherical wave. Since spherical waves propagate isotropically in space, there is a light wave component traveling in the direction of the observation point Q. Therefore, the optical wave reaching point Q is the superposition of all optical wave components generated on the spherical surface including point P. The phenomenon that optical waves wrap around like this is called diffraction.

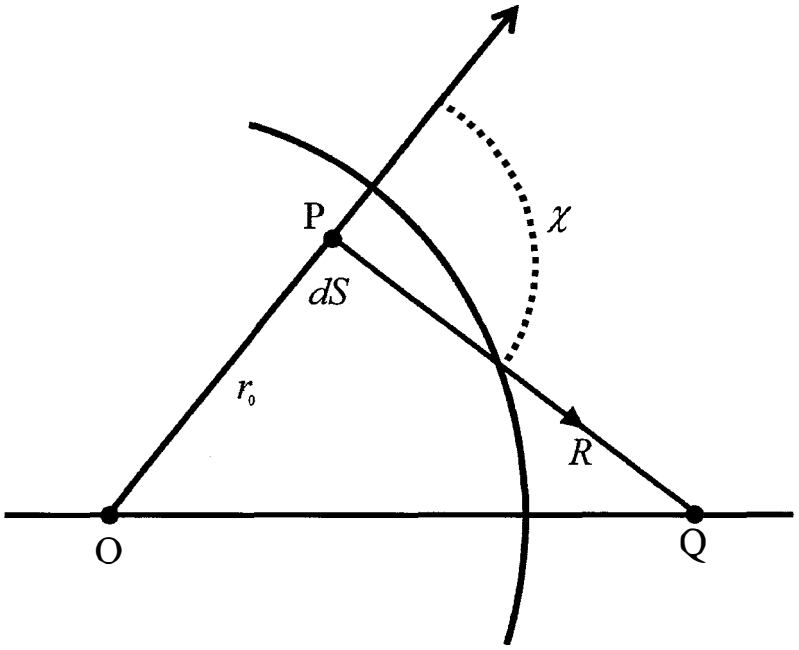

Fig. 2.3 Diffraction phenomenon.

The spherical wave that propagates the distance R from the point light source is expressed as

$$V(\mathrm{P},t)=\frac{a}{r_0}\exp\left[i(kr_0-\omega t+\phi)\right]. \tag{2.31}$$

Since the diffraction phenomenon does not deal with the passage of time, the optical wave is represented by a complex amplitude. The complex amplitude that is the coefficient of the temporal vibration term is

$$U(\mathrm{P};\omega)=\frac{a}{r_0}\exp\left[i(kr_0+\phi)\right]. \tag{2.32}$$

A secondary wave is generated from a small area dS (near point P) on a spherical surface of

radius r_0 centered on point O. The complex amplitude of the secondary wave reaching point Q is

$$dU(\mathrm{Q};\omega) = \frac{a}{r_0 R} K(\chi)\exp(ikr_0)\exp(ikR)dS, \tag{2.33}$$

considering the phase lag. Here, the initial phase at point O is $\phi = 0$. It is important to note that the secondary wave is generated from all over the spherical surface in Fig. 2.3, and the optical wave component that changes the direction of travel has its complex amplitude reduced and its ratio is represented by the inclination factor $K(\chi)$. In other word, the optical wave component that travels in the angular direction from the micro area dS shows the value, assuming that the complex amplitude is twice the original spherical wave.

Then, given that the point P is in a finite aperture, is given by

$$U(\mathrm{Q};\omega) = \int \frac{1+\cos\chi}{i2\lambda} \frac{a}{r_0 R}\exp\left[ik(r_0 + R)\right]dS, \tag{2.34}$$

by Frensnel-Kirchhoff's diffraction equation. Integration is over the diffractive sphere in the aperture. If the size of the aperture is small and the aperture center is on the straight line connecting the light source O and the observation point Q, $\cos(\chi)$ can be approximated as 1. Focusing on the fact that the optical wave distribution near the aperture is expressed as

$$U(\mathrm{P};\omega) = \frac{a}{r_0}\exp(ikr_0), \tag{2.35}$$

Eq. (2.34) is expressed as,

$$U(\mathrm{Q};\omega) = \frac{1}{i\lambda}\int U(\mathrm{P};\omega)\frac{1}{R}\exp(ikR)dS. \tag{2.36}$$

The optical wave at point Q is given by the composition of the optical wave generated by $U(\mathrm{P};\omega)$ on the aperture plane. Even if the optical wave distribution in the process of propagating to the aperture plane in unknown, the diffracted light reaching the observation point Q can be obtained if the complex amplitude $U(\mathrm{P};\omega)$ on the aperture plane is given.

The integration in Eq. (2.36) should be performed along the diffractive sphere centered at point O, but since χ can be approximated to be 0, it is performed over the same plane as the screen surface. Thus, Eq. (2.36) is simplified using some approximations, but it holds quite generally. These are summarized in Fig. 2.4 and the following Eq. (2.37). The light emitting surface is distributed near the optical axis on the x-y plane with $z = 0$. The complex

amplitudes are distributed in two dimensions, so they reach a point (X, Y) near the optical axis of $(z = z_0)$ of $U(\mathrm{P};\omega)$. If the amplitude distribution of the diffracted light is expressed as

$$U(X,Y,z_0;\omega) = \frac{1}{i\lambda}\int U(x,y,0;\omega)\frac{1}{R}\exp(ikR)d^2r_\perp, \tag{2.37}$$

where $d^2r_\perp = dxdy$. This is a basic equation that deals with diffraction phenomena. Here, R is the distance between the point (x, y) on the light source and the point (X, Y) on the observation surface, and the exponent is the phase delay due to the propagation of the optical wave there.

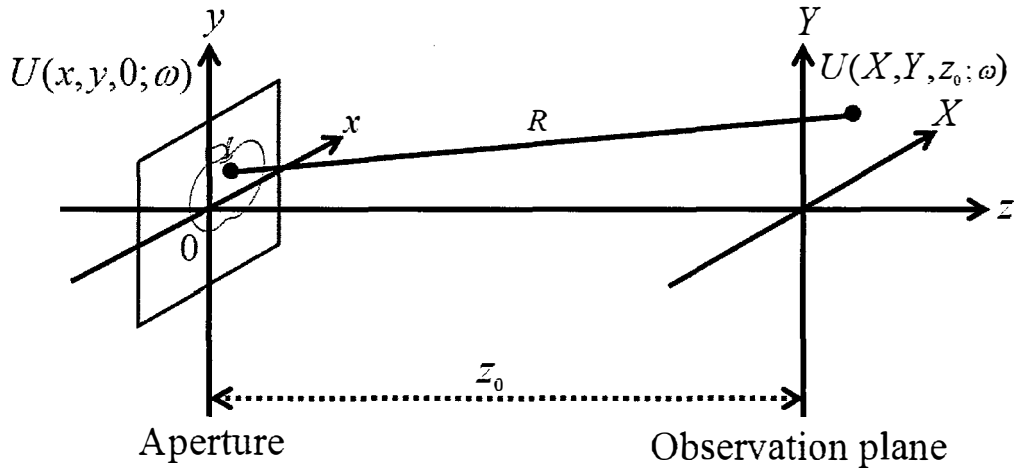

Fig. 2.4 Optical wave propagation.

2.4.2 Fresnel diffraction

The aperture at position $z = 0$ is shown in Fig. (2.4). When a plan wave is irradiated along the z-axis, the optical wave is diffracted by the aperture and reaches the observation plane $(z = z_0)$. The complex amplitude on the observation plane is given by the diffraction equation of Eq. (2.37). However, this formula looks simple, but it is difficult to perform the integration. The variable R included in the integral is the distance from each position (x, y) in the aperture to the observation point (X, Y). Therefore, the size of the aperture and the observation area are assumed to be sufficiently smaller than the distance z_0. Representing R in a Cartesian coordinate system,

$$R = z_0\left\{1+\left[\frac{(X-x)^2+(Y-y)^2}{z_0^{\,2}}\right]\right\}^{\frac{1}{2}}$$

$$= z_0 + \frac{(\rho_\perp - r_\perp)^2}{2z_0}, \tag{2.38}$$

where $\rho_\perp = (X, Y)$ and $r_\perp = (x, y)$. This is known as paraxial approximation. Equation (2.37) reduce to

$$U(\rho_\perp, z_0; \omega) = \frac{\exp(ikz_0)}{i\lambda z_0} \int U(r_\perp, 0; \omega) \exp\left\{\frac{ik}{2z_0}(\rho_\perp - r_\perp)^2\right\} d^2 r_\perp. \tag{2.39}$$

This diffraction phenomenon is called Fresnel diffraction.

2.5 Angular spectrum method

There exists an alternative treatment of the propagation of optical field, which is called the angular spectrum method. To begin, we consider a monochromatic field. The optical field is represented by the complex scalar function, $U(r_\perp, z; \omega)$. Throughout the space, the optical field satisfies the Helmholtz equation in Eq. (2.11)

$$(\nabla^2 + k^2) U(r_\perp, z; \omega) = 0, \tag{2.40}$$

where $k = \omega/c$. Let us define the position vectors $r_\perp = (x, y)$, where $r = (x, y, z) = (r_\perp, z)$.

To treat the propagation of the optical field, we express the optical field, $U(r_\perp, z; \omega)$ and $U(r_\perp, 0; \omega)$ on the aperture, as a two-dimensional (2D) Fourier integral with respect to $r_\perp$ as

$$U(r_\perp, z; \omega) = \frac{1}{2\pi} \int \tilde{U}(k_\perp, z; \omega) \exp(ik_\perp \cdot r_\perp) d^2 k_\perp, \tag{2.41}$$

$$U(r_\perp, 0; \omega) = \frac{1}{2\pi} \int \tilde{U}(k_\perp, 0; \omega) \exp(ik_\perp \cdot r_\perp) d^2 k_\perp, \tag{2.42}$$

where $\tilde{U}(k_\perp, z; \omega)$ is called the angular spectrum. $k = (k_x, k_y, k_z) = (k_\perp, k_z)$ is the wavenumber of the wavelength and $d^2 k_\perp = dk_x dk_y$. The optical field in the Fourier domain, $\tilde{U}(k_\perp, z; \omega)$, is related to the optical field in the spatial domain, $U(r_\perp, z; \omega)$ and $U(r_\perp, 0; \omega)$, via the inverse Fourier transform as

$$\tilde{U}(k_\perp, z; \omega) = \frac{1}{2\pi} \int U(r_\perp, z; \omega) \exp(-ik_\perp \cdot r_\perp) d^2 r_\perp. \tag{2.43}$$

$$\tilde{U}(k_\perp, 0; \omega) = \frac{1}{2\pi} \int U(r_\perp, 0; \omega) \exp(-ik_\perp \cdot r_\perp) d^2 r_\perp. \tag{2.44}$$

Substitution of Eq. (2.41) into Eq. (2.40) gives an equation that describes the z evolution of

the angular spectrum, $\tilde{U}(\boldsymbol{k}_\perp, z;\omega)$, as

$$\left(\frac{\partial^2}{\partial z^2}+k_z^2\right)\tilde{U}(\boldsymbol{k}_\perp, z;\omega)=0, \tag{2.45}$$

where

$$k_z=\begin{cases}\sqrt{k^2-\boldsymbol{k}_\perp^2} & \text{if} \quad (k_\perp \le k)\\ i\sqrt{\boldsymbol{k}_\perp^2-k^2} & \text{if} \quad (k_\perp \ge k)\end{cases} \tag{2.46}$$

is the z component of the wavenumber vector as a function of $\boldsymbol{k}_\perp$. Then, the angular spectrum, traveling in the direction of increasing z, obeys the propagation law

$$\tilde{U}(\boldsymbol{k}_\perp, z;\omega)=\exp(ik_z z)\tilde{U}(\boldsymbol{k}_\perp, 0;\omega). \tag{2.47}$$

Equation (2.46) implies that where $k_\perp \le k$, the waves are traveling waves and where $k_\perp \ge k$, the waves are evanescent waves. For our purposes, we ignore the evanescent waves. The function $\exp(ik_z z)$ in Eq. (2.47) is called the optical transfer function in free space. This equation (2.47) represents the relationship between the angular spectrum on a reference plane $z = \text{constant} > 0$ and that on the aperture $z = 0$.

Propagation law of the optical field in real space can be obtained by the Fourier transform of Eq. (2.47). If we take the paraxial approximation in the exponent of the optical transfer function, we obtain

$$\begin{aligned} k_z z &= \sqrt{k^2-\boldsymbol{k}_\perp^2}\, z \\ &= kz-\frac{\boldsymbol{k}_\perp^2}{2k}z. \end{aligned} \tag{2.48}$$

Then,

$$\exp(ik_z z)=\exp(ikz)\exp\left(-i\frac{\boldsymbol{k}_\perp^2}{2k}z\right). \tag{2.49}$$

The Fourier transform of this function gives

$$\begin{aligned} \frac{1}{2\pi}\int \exp(ik_z z)\exp\left[i(\boldsymbol{k}_\perp\cdot\boldsymbol{r}_\perp)\right]d^2k_\perp &= \frac{\exp(ikz)}{2\pi}\int \exp\left[-i\frac{\boldsymbol{k}_\perp^2}{2k}z+i(\boldsymbol{k}_\perp\cdot\boldsymbol{r}_\perp)\right]d^2k_\perp. \\ &= \frac{1}{i\lambda z}\exp\left(-i\frac{k}{2z}\boldsymbol{r}_\perp^2\right). \end{aligned} \tag{2.50}$$

Thus, the Fourier transform of Eq. (2.47) takes the form

$$U(\boldsymbol{r}_\perp, z;\omega) = \frac{1}{i\lambda z}\int U(\boldsymbol{r}'_\perp, 0;\omega)\exp\left[-i\frac{k}{2z}(\boldsymbol{r}_\perp - \boldsymbol{r}'_\perp)^2\right]d^2\boldsymbol{r}'_\perp . \tag{2.51}$$

This expression of the propagation law of optical field is equivalent to the Fresnel diffraction formula in Eq. (2.39).

2.6 Fourier transform spectroscopy

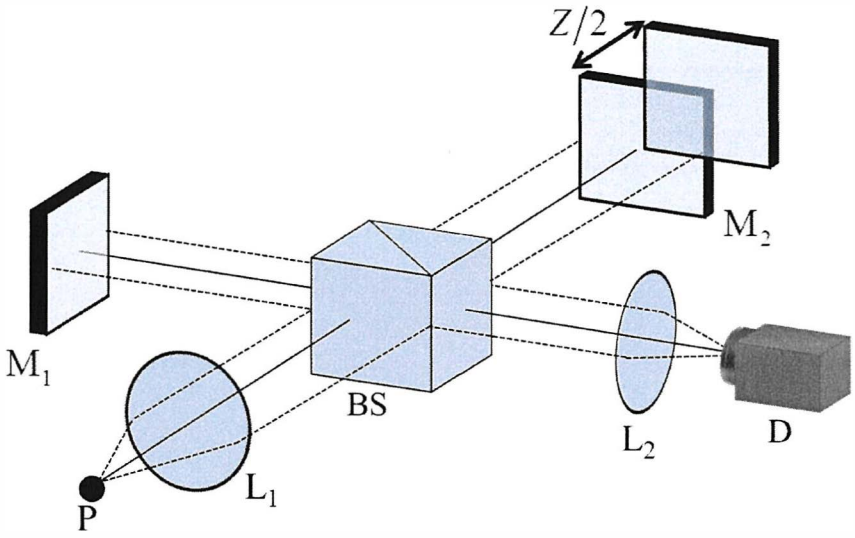

Fig. 2.5 Michelson interferometer

The coherence function of a light source can be measured by using a Michelson interferometer. Figure 2.5 shows a schematic of a Michelson interferometer. Consider a light source with a continuous spectrum and intensity distribution $S(\omega)$. Suppose a Michelson interferometer is illuminated with a light source. The light propagates from point P to lens L_1, where it is collimated onto the beam splitter (BS). At the BS, the collimated light is split into two parts (Fig. 2.5). Each split wavefront is reflected by either mirror M_1 or M_2. The optical waves are superposed on the BS again. Each frequency component produces an interference pattern. Lens L_2 focuses the light on the detector D. The detector records the intensity distribution, which is given by

$$I(\boldsymbol{r}) = \frac{1}{4}\left[2\Gamma(\boldsymbol{r},0) + \Gamma\left(\boldsymbol{r},\frac{Z}{c}\right) + \Gamma^{*}\left(\boldsymbol{r},\frac{Z}{c}\right)\right]$$
$$= \frac{1}{2}\int_0^\infty S(\boldsymbol{r};\omega)d\omega + \frac{1}{4}\int_0^\infty S(\boldsymbol{r};\omega)\exp\left(i\omega\frac{Z}{c}\right)d\omega + \frac{1}{4}\int_0^\infty S(\boldsymbol{r};\omega)\exp\left(-i\omega\frac{Z}{c}\right)d\omega$$
$$= \frac{c}{2}\int_0^\infty S(\boldsymbol{r};ck)dk + \frac{c}{2}\int_0^\infty S(\boldsymbol{r};ck)\cos(kZ)dk, \tag{2.52}$$

since the time difference is $\tau = Z/c$. In this equation, the first term is a constant term, where $S(\boldsymbol{r};ck)$ is the time-averaged intensity of each optical wave, and the second term represents the interference between two optical waves and can be considered as a positive or negative deviation from the constant term that depends on the path difference, Z. The intensity fluctuation about the constant bias forms the spectral distribution, given by

$$I(Z) = \frac{c}{2}\int_0^\infty S(\boldsymbol{r};ck)\cos(kZ)dk. \tag{2.53}$$

The interferogram is obtained by detecting the output intensity, $I(Z)$, as a function of path difference Z at a point on the optical axis of the system. Then, by taking the Fourier transform of the interferogram, the spectral irradiance distribution, $S(\boldsymbol{r};ck)$, is found as a function of wavenumber as

$$S(\boldsymbol{r};ck) = \frac{4}{\pi c}\int_0^\infty I(Z)\cos(kZ)dZ. \tag{2.54}$$

The minimum resolvable wavelength interval is given by

$$\Delta\lambda = \frac{\lambda^2}{l_z}, \tag{2.55}$$

where l_z is the total path difference.

2.7 Summary

The mathematical expression of the behavior of light can be obtained from Maxwell's equations. Interference is a property of optical waves that is based on the superposition principle. The mathematical representation of interference between two optical waves has three terms to consider. The first two terms are constant terms that depend on the intensities of the individual optical waves. The last term is the interference term that depends on the

interference between the two optical waves and was used to confirm the wave nature of light. The interference term depends on the coherence of the optical waves, and there are temporal and spatial coherence functions. Coherence can be identified by the degree of coherence or by a normalized space-time correlation function. Temporal coherence length can be measured by a Michelson interferometer and the spectral distribution of the light source can be revealed by taking a Fourier transform of an interferogram.

The treatment of the wave propagation by angular spectrum method was described. Propagation of the angular spectrum is performed by the optical transfer function. Under the paraxial approximation, it gives mathematically the same expression as in the Fresnel diffraction formula.

III Multispectral incoherent holographic

3.1 Introduction

In this chapter, the concept of multispectral incoherent holography is outlined. First, the measurement system is introduced, which measures the differential wavefront curvature between two split wavefronts. The system obtains a volume (3D) interferogram that records a 3D spatial correlation function. The signal processing procedure for spectral decomposition to obtain a set of complex incoherent holograms for different spectral components is described. The 3D image at each spectrum can be reconstructed from the complex incoherent hologram by applying conventional inverse propagation techniques.

3.2 Measurement of 3D volume interferogram

Figure 3.1 shows a schematic of the optical system. This system is similar to a Michelson interferometer, but one of the mirrors is replaced with a concave mirror. The origin of Cartesian coordinate system is set close to the measured 3D object. This object, assumed to be polychromatic and spatially incoherent, is localized within a finite volume $\sum$ centered at the origin. The optical wave that is propagated from the object is divided into two parts by the beam splitter (BS). Each split wavefront is reflected by either a concave mirror (M_1) of focal length f_1 or plane mirror (M_2). Those optical waves are superposed on the BS again. A 2D interference pattern, $I(\rho_\perp)$, is created and recorded by the image sensor (D). Here, $\rho_\perp = (X, Y)$ is the 2D coordinate system across the observation plane. The optical path difference, Z, between the two wavefronts is introduced by moving the piezoelectric translator (PZT) along the optical axis stepwise. The 2D interferogram at each position of the PZT is recorded. This procedure is like that of Fourier transform spectrometry. The recorded data create a 3D volume interferogram. We write $\rho = (\rho_\perp, Z) = (X, Y, Z)$ as the coordinate system taken in the volume interferogram. Let the distance between M_1 and D be d_1 and let the distance between M_2 and the origin of Cartesian coordinate system be $d_0 + Z/2$, and defining the distance between D and the origin of Cartesian coordinate system as $z_0 = d_0 + d_1$,

the optical intensity of volume interferogram, $I(\rho)$, is given by

$$I(\rho) = \left\langle \left| V_1(\rho_\perp, z_0, t) + V_2(\rho_\perp, z_0 + Z, t) \right|^2 \right\rangle$$

$$= \frac{1}{4}\left[\Gamma_{11}(\rho_\perp) + \Gamma_{22}(\rho) + \Gamma_{12}(\rho) + \Gamma_{12}^*(\rho) \right], \tag{3.1}$$

where the angle brackets indicate an ensemble average and the asterisk denotes a complex conjugate. We suppress the time t in Γ because the optical field is assumed to be stationary in time. In Eq. (3.1), $\Gamma_{11}(\rho_\perp) = \left\langle \left| V_1(\rho_\perp, z_0, t) \right|^2 \right\rangle$ and $\Gamma_{22}(\rho) = \left\langle \left| V_2(\rho_\perp, z_0 + Z, t) \right|^2 \right\rangle$ are the optical intensities of optical fields $V_1(\rho_\perp, z_0, t)$ reflected by the concave mirror and $V_2(\rho_\perp, z_0 + Z, t)$, reflected by the plane mirror. The 3D spatial correlation function, $\Gamma_{12}(\rho) = \left\langle V_1^*(\rho_\perp, z_0, t)\, V_2(\rho_\perp, z_0 + Z, t) \right\rangle$, of the optical field contains both 3D spatial information and spectral information of the polychromatic object.

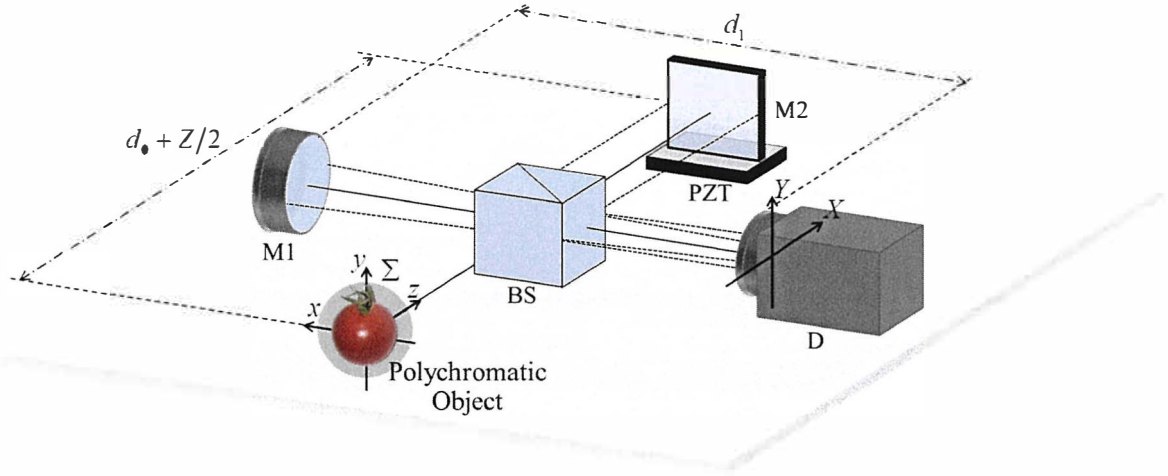

Fig. 3.1 Schematic of optical system. BS: beam splitter, M1: concave mirror, M2: plane mirror; and D: image sensor. The optical distance between M1 and D is d_1, the optical distance between M2 and the origin of Cartesian coordinate system is $d_0 + Z/2$, and the optical distance between D and origin of Cartesian coordinate system is $z_0 = d_0 + d_1$. The optical path difference, Z, is introduced by the PZT.

3.3 Reconstruction of 3D images for many spectral components

The spatial correlation function $\Gamma_{12}(\rho)$ for the stationary optical field recorded in the volume interferogram is expressed as a superposition of the cross spectral density function, W_{12}, in the form

$$\Gamma_{12}(\rho) = \int_0^\infty W_{12}(\rho;\omega)\,d\omega, \tag{3.2}$$

where $\omega = ck$ is the angular frequency, c is the speed of light in free space, and $k = 2\pi/\lambda$ is the wavenumber of wavelength λ. Equation (3.2) is a special case of the Wiener-Khinchin theorem, in which temporal difference is set to be zero. This equation means that for a stationary optical field, spectral components of the optical fields for different frequencies are mutually uncorrelated. The cross-spectral density function on the right-hand side of Eq. (3.2) is defined as the cross-correlation of monochromatic components U_1 and U_2 of V_1 and V_2 as

$$W_{12}(\rho;\omega) = \left\langle U_1^*(\rho_\perp, z_0;\omega)\; U_2(\rho_\perp, z_0 + Z;\omega)\right\rangle. \tag{3.3}$$

Under the paraxial approximation and the assumption $z_0 >> Z$, this cross-spectral density function can be written as

$$W_{12}(\rho;\omega) = W_{12}^{(z_0)}(\rho_\perp;\omega)\exp(ikZ), \tag{3.4}$$

where

$$W_{12}^{(z_0)}(\rho_\perp;\omega) = \left\langle U_1^*(\rho_\perp, z_0;\omega)\; U_2(\rho_\perp, z_0;\omega)\right\rangle \tag{3.5}$$

is the cross-spectral density function defined over the observation plane $z = z_0$. Substituting Eq. (3.4) into Eq. (3.2) gives the relationship between the spatial correlation function Γ_{12}, and the cross-spectral density function across the observation plane as

$$\Gamma_{12}(\rho) = c\int_0^\infty W_{12}^{(z_0)}(\rho_\perp;\omega)\exp(ikZ)\,dk. \tag{3.6}$$

It is then clear that Eq. (3.6) may be inverted to express the cross-spectral density function across the observation plane as the Fourier transform of the spatial correlation function,

$$W_{12}^{(z_0)}(\rho_\perp;\omega) = \frac{1}{2\pi c}\int \Gamma_{12}(\rho)\exp(-ikZ)\,dZ. \tag{3.7}$$

In Eq. (3.7), the integrand has taken over the actual extension of the interferogram with respect to Z.

From Eq. (3.1), the 3D interferogram being recorded includes two intensity distribution terms and two interference terms. These interference terms can be separated from the intensity distribution terms during the retrieval of the cross-spectral density functions because cross-correlation term $\Gamma_{12}(\rho)$ contains only positive-frequency spectral components, as shown in the integral region in Eq. (3.6), and $\Gamma_{12}^{*}(\rho)$ contains only negative-frequency components. On the other hand, the intensity distribution terms Γ_{11} and Γ_{22} do not change rapidly within the volume interferogram. This means that the spectra of Γ_{11} and Γ_{22} appear close to the zero spatial-frequency region, separate from those of Γ_{12} and Γ_{12}^{*}. By choosing the positive frequency components, we obtain the information of Γ_{12}, separated from other terms.

3.4 Propagation of optical coherence from spatially incoherent source

The cross-spectral density function, $W_{12}^{(z_0)}(\rho_\perp;\omega)$, across the observation plane in Eq. (3.5) is defined as the cross correlation of the monochromatic component of the optical field, $U_1(\rho_\perp, z_0;\omega)$ and $U_2(\rho_\perp, z_0;\omega)$. The optical field $U_2(\rho_\perp, z_0;\omega)$ is expressed as a superposition of the spherical wave propagated from a point $\boldsymbol{r}_s = (x_s, y_s, z_s) = (\boldsymbol{r}_{s\perp}, z_s)$ on the 3D object to the observation plane $z = z_0 = d_0 + d_1$, and is written as

$$U_2(\rho_\perp, z_0;\omega) = \int_{\Sigma} \frac{A(\boldsymbol{r}_{s\perp}, z_s)}{R}\exp(ikR)d^3r_s. \tag{3.8}$$

Here, $A(\boldsymbol{r}_{s\perp}, z_s)$ is the amplitude at the point $\boldsymbol{r}_s$ and R is the distance between the point on the object $\boldsymbol{r}_s$ and the point $(\rho_\perp, z_0) = (X, Y, z_0)$ on the observation plane. Under the paraxial approximation, R may be expressed as

$$R = \sqrt{(\rho_\perp - \boldsymbol{r}_{s\perp})^2 + (z_0 - z_s)^2}$$

$$= z_0 - z_s + \frac{(\boldsymbol{\rho}_\perp - \boldsymbol{r}_{s\perp})^2}{2(z_0 - z_s)}, \tag{3.9}$$

where $z_0 - z_s$ is the optical distance of the point $\boldsymbol{r}_s$, as measured from the observation plane. Substitution of Eq. (3.9) into Eq. (3.8) gives the following expression of the optical field $U_2(\boldsymbol{\rho}_\perp, z_0; \omega)$,

$$U_2(\boldsymbol{\rho}_\perp, z_0; \omega) = \frac{1}{z_0} \int_\Sigma \exp\left[ik(z_0 - z_s)\right] A(\boldsymbol{r}_{s\perp}, z_s) \exp\left[\frac{ik}{2(z_0 - z_s)}(\boldsymbol{\rho}_\perp - \boldsymbol{r}_{s\perp})^2\right] d^3 r_s, \tag{3.10}$$

where we omit z_s in the numerator because $z_0 >> z_s$. To obtain the expression of $U_1(\boldsymbol{\rho}_\perp, z_0; \omega)$, we consider the optical field, $U_1(\boldsymbol{r}'_\perp, d_0; \omega)$, across the plane $z = d_0$ in front of the concave mirror. Replacing z_0 by d_0 in Eq. (3.10), we obtain

$$U_1(\boldsymbol{r}'_\perp, d_0; \omega) = \frac{1}{d_0} \int_\Sigma \exp\left[ik(d_0 - z'_s)\right] A(\boldsymbol{r}'_{s\perp}, z'_s) \exp\left[\frac{ik}{2(d_0 - z'_s)}(\boldsymbol{r}'_\perp - \boldsymbol{r}'_{s\perp})^2\right] d^3 r'_s. \tag{3.11}$$

Then, the optical field immediately after reflecting by the concave mirror of focal length f_1 is expressed as

$$U'_1(\boldsymbol{r}'_\perp, d_0; \omega) = U_1(\boldsymbol{r}'_\perp, d_0; \omega) \exp\left[-\frac{ik}{2f_1} \boldsymbol{r}'^2_\perp\right]. \tag{3.12}$$

The optical field $U_1(\boldsymbol{\rho}_\perp, z_0; \omega)$ is related with $U'_1(\boldsymbol{r}'_\perp, d_0; \omega)$ by the usual propagation law for the distance d_1,

$$U_1(\boldsymbol{\rho}_\perp, z_0; \omega) = \frac{1}{i\lambda} \frac{\exp(ikd_1)}{d_1} \int_\Sigma \int U'_1(\boldsymbol{r}'_\perp, d_0; \omega) \exp\left[\frac{ik}{2d_1}(\boldsymbol{\rho}_\perp - \boldsymbol{r}'_\perp)^2\right] d^2 r'_\perp d^3 r'_s. \tag{3.13}$$

Substituting Eqs. (3.12) and (3.11) into Eq. (3.13), and carrying out the integration by $\boldsymbol{r}'_\perp$, we may write the optical field across the observation plane after modulating by the concave mirror as

$$U_1(\boldsymbol{\rho}_\perp, z_0; \omega) = \frac{f_1}{f_1 z_0 - d_0 d_1} \int_\Sigma \exp\left[ik(z_0 - z'_s)\right] A(\boldsymbol{r}'_{s\perp}, z_s; \omega)$$

$$\times \exp\left[\frac{ik}{2} \frac{f_1 - (d_0 - z_s)}{f_1 d_1 + (f_1 - d_1)(d_0 - z_s)} \left(\boldsymbol{\rho}_\perp - \frac{f_1}{f_1 - (d_0 - z_s)} \boldsymbol{r}'_{s\perp}\right)^2\right]$$

$$\times \exp\left[-\frac{ik}{2}\frac{1}{f_1-(d_0-z_s)}\boldsymbol{r}_{s\perp}'^{\,2}\right]d^3\boldsymbol{r}_s'. \tag{3.14}$$

On substituting Eqs. (3.10) and (3.14) into Eq. (3.5), and changing order of integration and averaging, we may write the cross-spectral density function in Eq. (3.5) as

$$\begin{aligned} W_{12}^{(z_0)}(\boldsymbol{\rho}_\perp;\omega) = {} & \frac{f_1}{z_0(f_1z_0-d_0d_1)}\int_\Sigma \exp\left[ik(z_s-z_s')\right]\left\langle A^*(\boldsymbol{r}_{s\perp}', z_s')A(\boldsymbol{r}_{s\perp}, z_s)\right\rangle \\ & \times \exp\left[\frac{ik}{2(z_0-z_s)}(\boldsymbol{\rho}_\perp-\boldsymbol{r}_{s\perp})^2\right] \\ & \times \exp\left[-\frac{ik}{2}\frac{f_1-(d_0-z_s)}{f_1d_1+(f_1-d_1)(d_0-z_s)}\left(\boldsymbol{\rho}_\perp-\frac{f_1}{f_1-(d_0-z_s)}\boldsymbol{r}_{s\perp}'\right)^2\right] \\ & \times \exp\left[\frac{ik}{2}\frac{1}{f_1-(d_0-z_s)}\boldsymbol{r}_{s\perp}'^{\,2}\right]d^3\boldsymbol{r}_s d^3\boldsymbol{r}_s'. \end{aligned} \tag{3.15}$$

Because the measured object is incoherent in space, the amplitudes at different points on the object are mutually uncorrelated. Thus,

$$\left\langle A^*(\boldsymbol{r}_{s\perp}', z_s')A(\boldsymbol{r}_{s\perp}, z_s)\right\rangle = S(\boldsymbol{r}_{s\perp}, z_s)\delta^2(\boldsymbol{r}_{s\perp}-\boldsymbol{r}_{s\perp}')\delta(z_s-z_s'). \tag{3.16}$$

Substituting Eq. (3.16) into Eq. (3.15) and intregrating by $\boldsymbol{r}_s'$, we obtain the final expression of the cross-spectral density function as

$$W_{12}^{(z_0)}(\boldsymbol{\rho}_\perp;\omega) = \kappa\int_\Sigma S(\boldsymbol{r}_{s\perp}, z_s)\exp\left[\frac{ik}{2}\frac{1}{\gamma(z_s)}(\boldsymbol{\rho}_\perp-m\boldsymbol{r}_{s\perp})^2\right]d^3\boldsymbol{r}_s, \tag{3.17}$$

$$\kappa = \frac{f_1}{z_0(f_1z_0-d_0d_1)}, \tag{3.18}$$

$$\frac{1}{\gamma(z_s)} = \frac{(d_0-z_s)^2}{(d_1+d_0-z_s)\left[f_1d_1+(f_1-d_1)(d_0-z_s)\right]}, \tag{3.19}$$

$$m = -\frac{d_1}{d_0-z_s}. \tag{3.20}$$

Here, κ is a coefficient, $\boldsymbol{r}_s=(\boldsymbol{r}_{s\perp}, z_s)=(x_s, y_s, z_s)$ is a point on the polychromatic object, $\gamma(z_s)$ is the radius of the differential wavefront curvature as a function of z_s, and m is the lateral magnification.

3.5 Reconstruction of 3D image

Equation (3.7) allows us to retrieve the cross-spectral density function across the observation plane. This cross-spectral density function, which is expressed as Eq. (3.17), is equivalent to the complex incoherent hologram of a spectral component. Thus, the 3D image for each spectrum can be reconstructed from the complex incoherent hologram by applying the usual inverse propagation formula,

$$O(\boldsymbol{r}_\perp, z; \omega) = W_{12}^{(z_0)}(\boldsymbol{\rho}_\perp; \omega) \otimes \exp\left[-\frac{ik}{2\gamma(z)}\boldsymbol{\rho}_\perp^{\,2}\right], \tag{3.21}$$

where, $\otimes$ is the convolution integral. Or, it can be expressed explicitly as

$$O(\boldsymbol{r}_\perp, z; \omega) = \int W_{12}^{(z_0)}(\boldsymbol{\rho}_\perp; \omega) \exp\left[-\frac{ik}{2\gamma(z)}(\boldsymbol{\rho}_\perp - \boldsymbol{r}_\perp)^2\right] d^2\rho_\perp . \tag{3.22}$$

The objects that are located across plane $z = z_s$ are in focused and other objects are defocused.

3.6 Summary

In this chapter, we show the interferometer used in this study. The relationship between the volume interferogram and the spatial correlation function can be obtained from this measurement method. Next, the cross-spectral density function across the observation plane can be expressed as the Fourier transform of the spatial correlation function. The spectral profile of the object is also obtained.

This cross-spectral density function is equivalent to the complex incoherent hologram of spectral component. Thus, we can reconstruct the 3D image for each spectrum from the complex incoherent hologram by applying the usual inverse propagation formula.

IV Experiment

4.1 Introduction

This chapter presents the experimental conditions and results. The object being measured is polychromatic. An interferometer is used to measure the volume interferogram. The spectral profiles of the objects and the complex incoherent hologram for each spectral component are obtained by applying a Fourier transform to this volume interferogram with respect to the optical path difference, Z. The performance of the method for reconstructing multispectral images is discussed.

4.2 Experiment 1

4.2.1 Experimental conditions

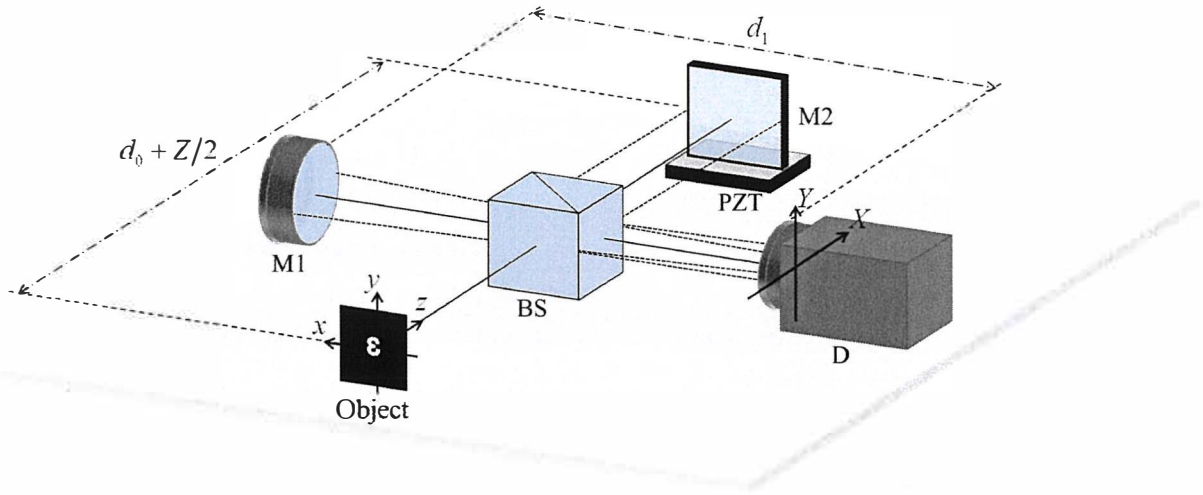

Fig. 4.1 Schematic of the experiment setup.

The optical distance between M2 and the origin of the Cartesian coordinate system is $d_0 + Z/2$, the optical distance between M1 and D is d_1, and the optical path difference, Z, is introduced by the PZT. BS: beam splitter, M1: concave mirror, M2: plane mirror; and D: image sensor.

In this section the experiment used to obtain the volume interferogram is described. A schematic of the experimental setup is shown in Fig. 4.1. The measured object is a mask screen of the number 3 that is illuminated from behind by a metal halide lamp (MHL) as a white light source, so that the measured object is a planar polychromatic object. Figure 4.2 shows the spectral profile of the MHL obtained by Fourier transform spectrometry. The spectral resolution is 61.09 cm^{-1} and the spectral range is 3.13×10^4 cm^{-1}. Figure 4.3 shows a photograph of the mask screen, which is 0.8×0.9 mm in size. Other parameters are listed in Table 4.1.

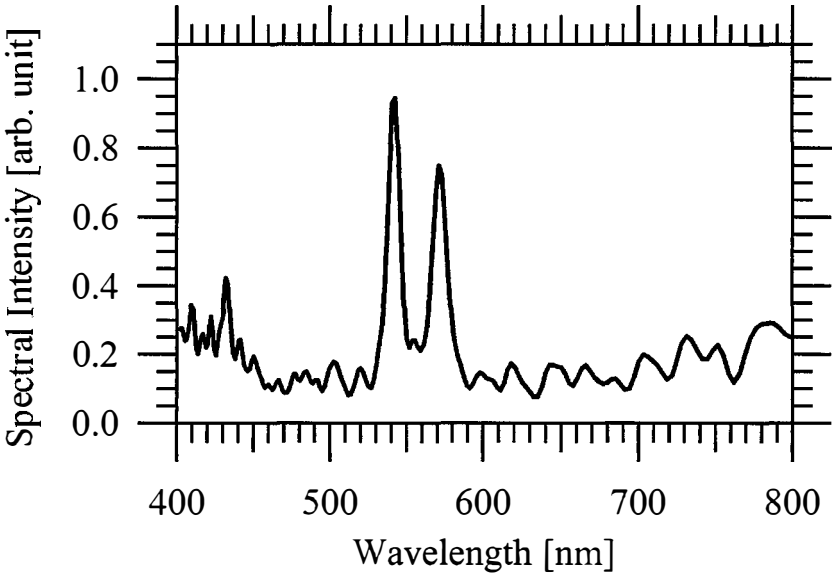

Fig. 4.2 Spectral profile of the MHL measured by Fourier transform spectrometry.

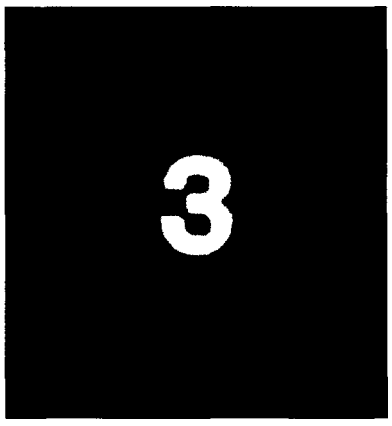

Fig. 4.3 Photograph of the mask screen of the number 3.

Table 4.1. System settings for experiment 1.

Parameter		
	d_0	100 mm
	d_1	120 mm
	f_1	524 mm
	z_s	0 mm
PZT	Number of steps	256
	Step interval	80 nm
D	Number of pixels	1024 square
	Pixel size	6.9 μm

4.2.2 Experimental results

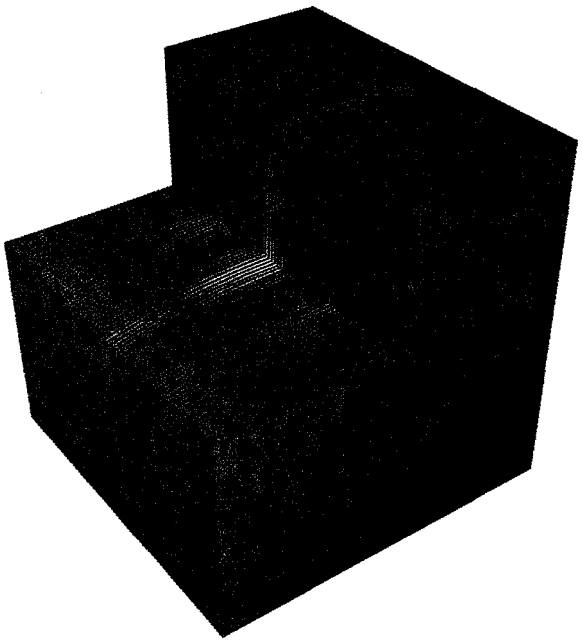

Fig. 4.4 Volume interferogram obtained in experiment 1.

Figure 4.4 shows the volume interferogram obtained in experiment 1. A quarter of the interferogram has been omitted to show the inner fringe arrangement. Figure 4.5 shows the intensity distribution of the volume interferogram along the optical path difference, *Z*, at the center point of the interference fringe space. Figure 4.6 shows the continuous spectral profile of the object. This spectral profile is obtained by taking the Fourier transform of the intensity

distribution in Fig. 4.5. The number of data points is 53, which covers the wavelength range of visible light. The spectral resolution is limited by the step interval and number of steps of the PZT. A spectral peak is located at 538.9 nm, and the spectral resolution at the wavelength is 7.11 nm. Within the spectral resolution, the spectral profile agrees with that in Fig. 4.2.

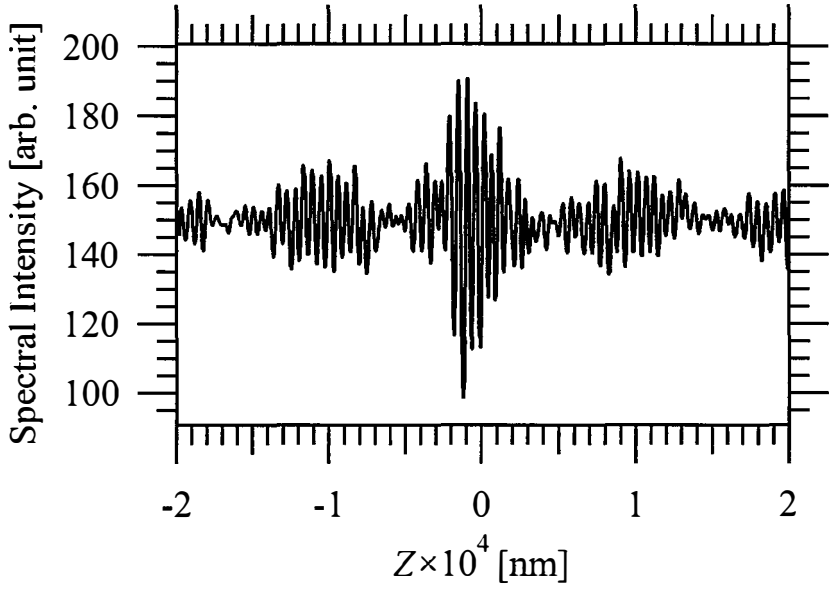

Fig. 4.5 Intensity distribution of the volume interferogram along the optical path difference, Z, at the center point of the interference fringe space.

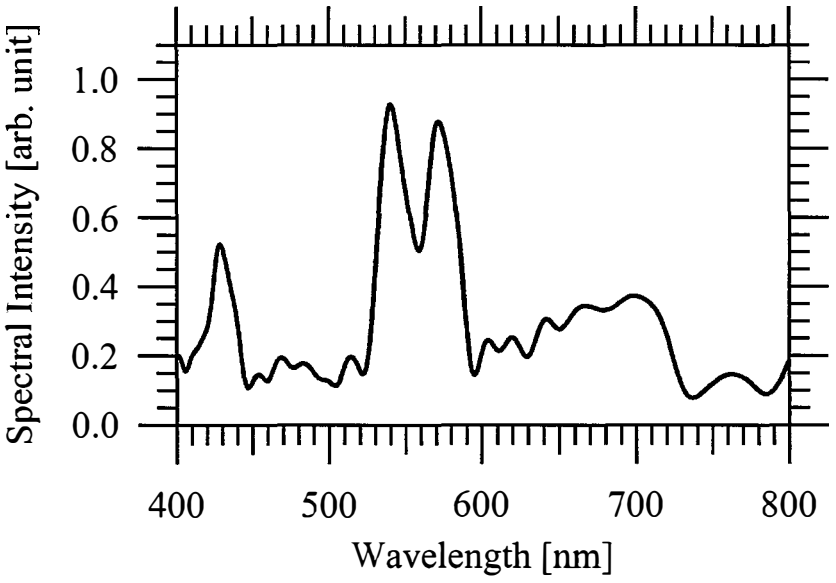

Fig. 4.6 Continuous spectral profile recorded on the observation plane by taking the Fourier transform of the intensity distribution in Fig. 4.5.

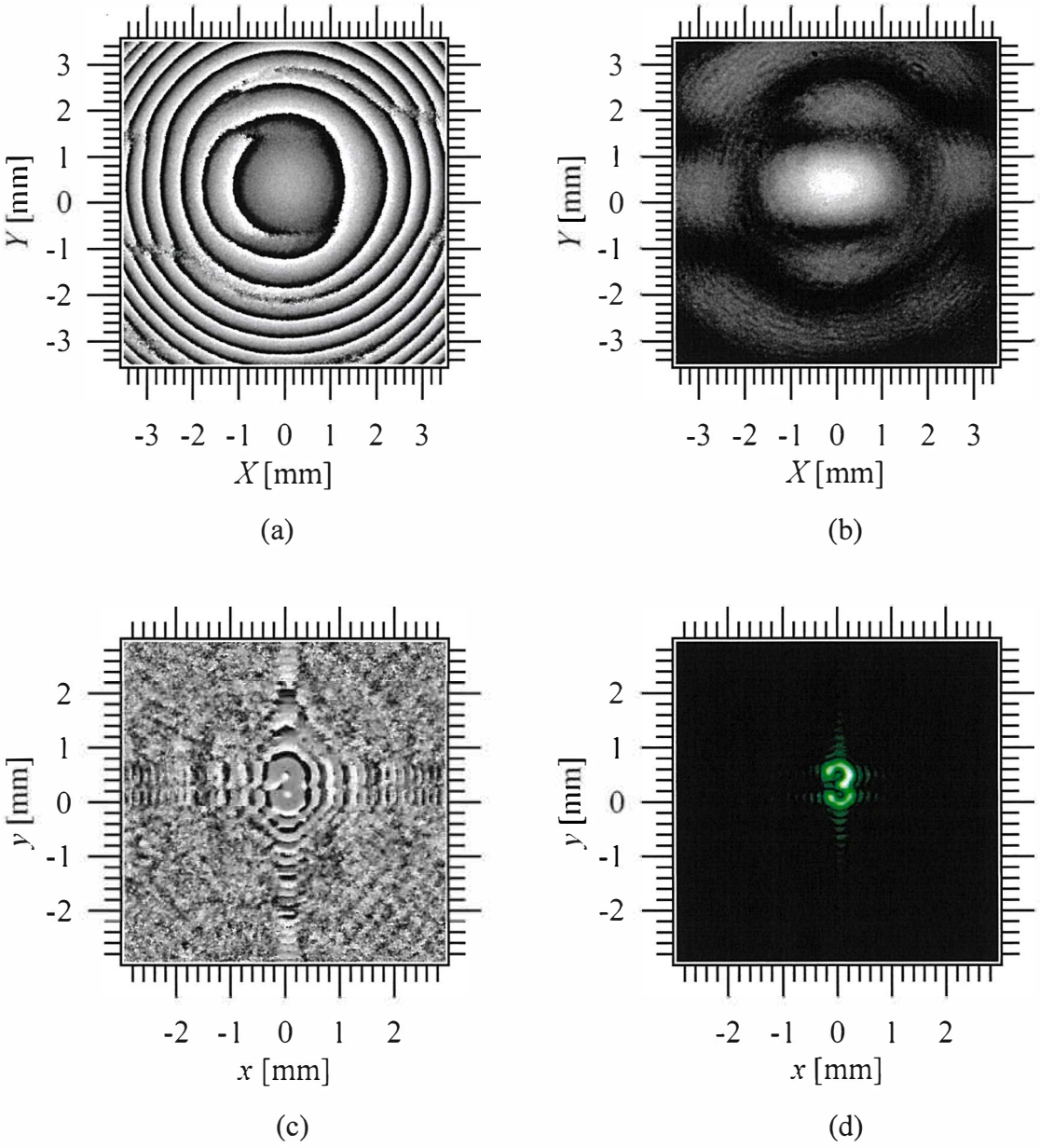

Fig. 4.7 (a) Phase distribution and (b) absolute value of the complex incoherent hologram at spectral peak $\lambda = 538.9$ nm. (c) Phase distribution of the reconstructed image and (d) in-focus image over the *x*-*y* plane at $z = -1$ mm.

Figure 4.7(a)–(d) show the complex incoherent hologram at $\lambda = 538.9$ nm. Figure 4.7(a) shows the phase distribution and Fig. 4.7(b) shows the absolute value of the complex incoherent hologram. Figure 4.7(c) shows the phase distribution of the reconstructed image and Fig. 4.7(d) shows the in-focus image over the *x*-*y* plane, where the reconstruction distance is $z = -1$ mm. The shape of the measured object is reconstructed and the size of the number 3 is close to the original size of the 3 in Fig. 4.3. Figures 4.8(a) and (b) show the intensity

distributions over the *x*-*z* and *y*-*z* planes and Fig. 4.8(c) shows the intensity profile along the *z*-direction at $\lambda = 538.9$ nm. The intensity peak is close to $z = -1$ mm, which is in agreement with object position $z_s = 0$ mm.

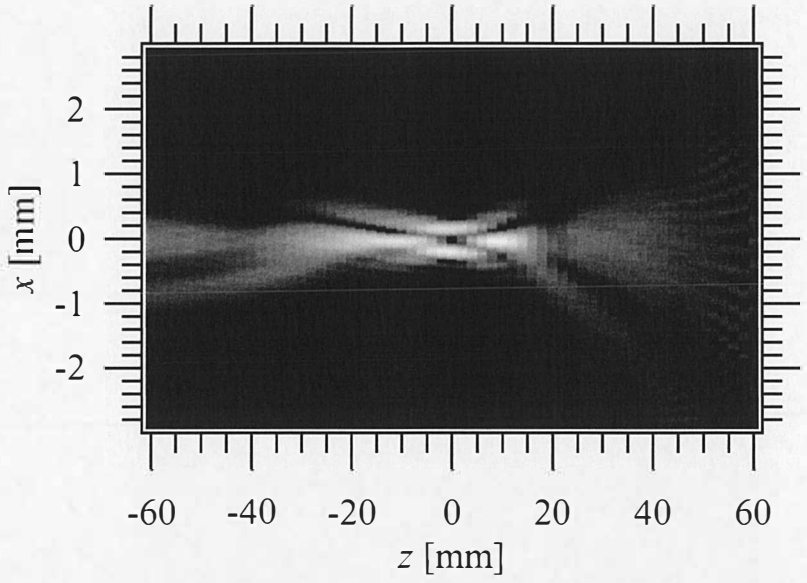

(a)

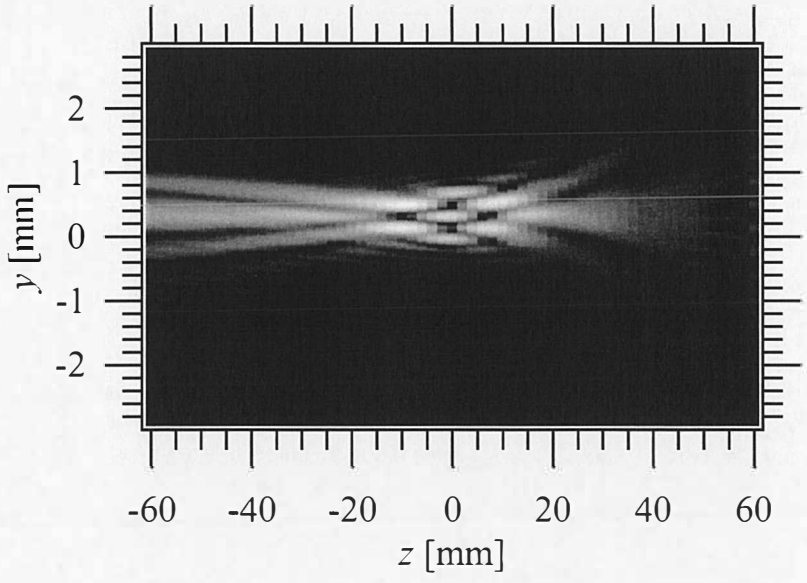

(b)

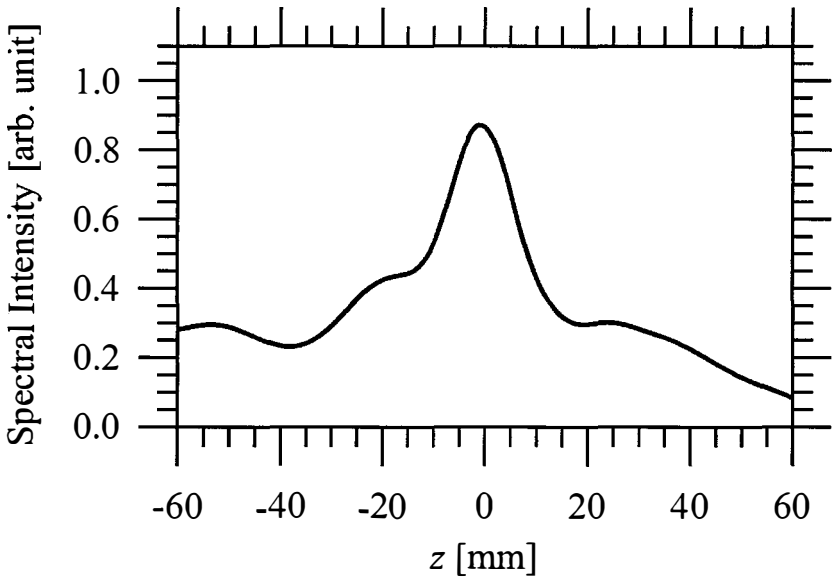

(c)

Fig. 4.8 Intensity distribution of the number 3 mask screen over the (a) x-z and (b) y-z planes. (c) Intensity profile of the reconstructed image along the z-direction at $\lambda = 538.9$ nm.

4.3 Experiment 2

4.3.1 Experimental conditions

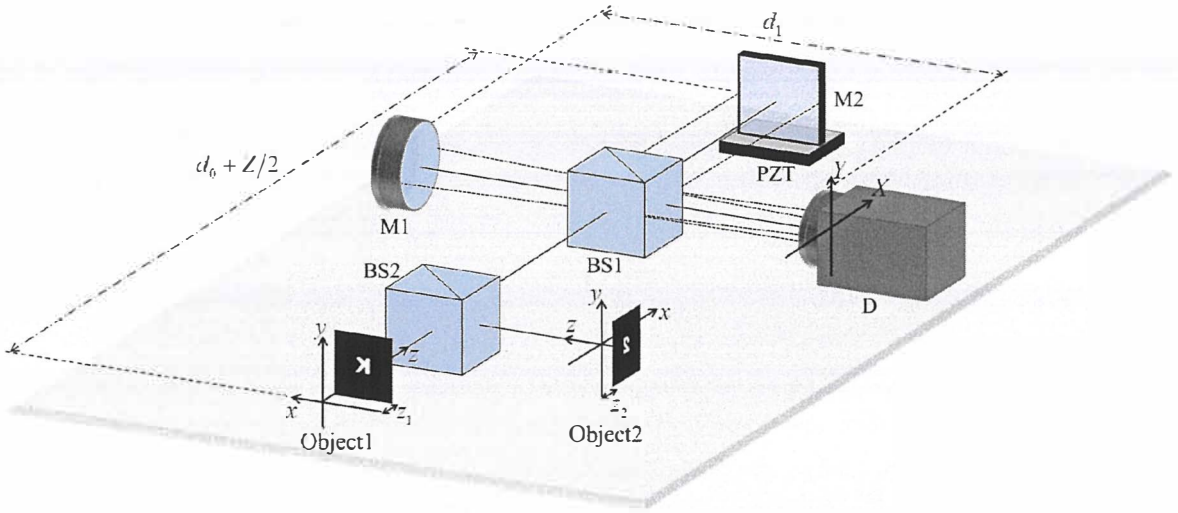

Fig. 4.9 Schematic of the experimental setup. The origin of the Cartesian coordinate system is set between object 1 and object 2.

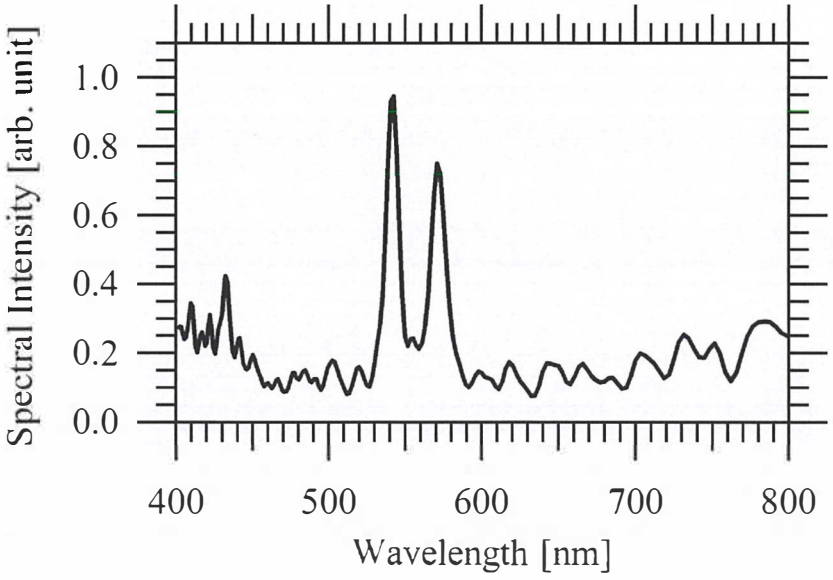

(a)

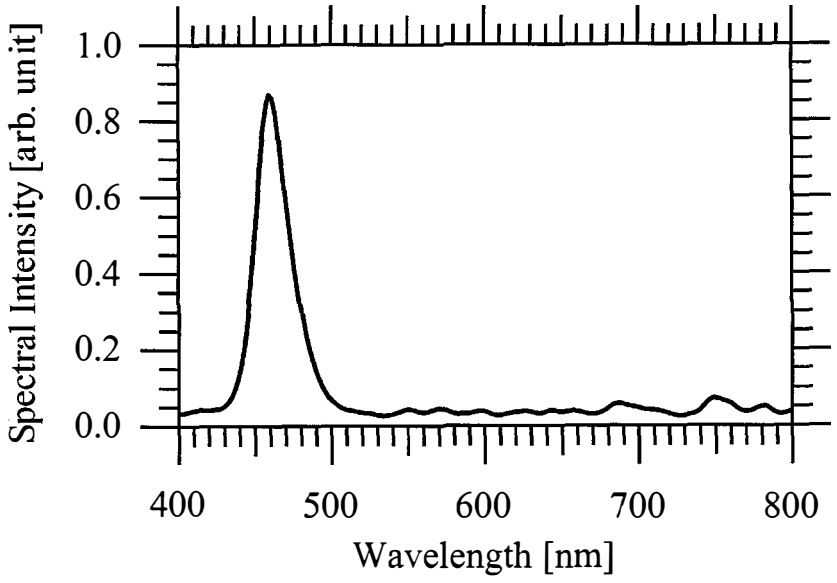

(b)

Fig. 4.10 Spectral profiles of the (a) MHL and (b) blue LED light sources measured by Fourier transform spectrometry.

This section describes the experiment in which a set of the spectral components of the 3D images is obtained. The measured objects are two mask screens of the letter K and number 2 that are illuminated by incoherent light sources, namely an MHL and a blue LED, so that the measured objects are planar polychromatic objects located at different depths (Fig. 4.9).

(a) (b)

Fig. 4.11 Photographs of the mask screens. (a) K (0.8 × 0.8 mm) and (b) 2 (0.7 × 0.8 mm) mask screens.

Figure 4.10 shows the spectral profiles of the MHL and blue LED, which were measured separately by Fourier transform spectrometry. The spectral resolution was 61.09 cm^{-1} and the spectral range was 3.13×10^4 cm^{-1}. Figure 4.11 shows photographs of the K (0.8 × 0.8 mm) and 2 (0.7 × 0.8 mm) mask screens. Other parameters are listed in Table 4.2.

Table 4.2. System settings for experiment 2

Parameter		
	d_0	160 mm
	d_1	120 mm
	f_1	524 mm
	z_1	5 mm
	z_2	-5 mm
PZT	Number of steps	256
	Step interval	80 nm
D	Number of pixels	1024 square
	Pixel size	6.9 μm

4.3.2 Experimental results

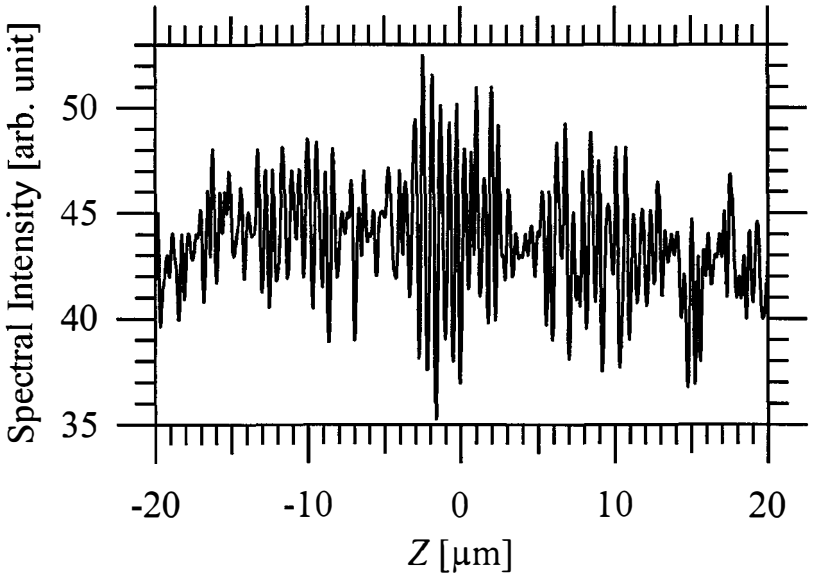

Fig. 4.12 Intensity distribution at point (X, Y) of the volume interferogram plotted with respect to optical path difference Z.

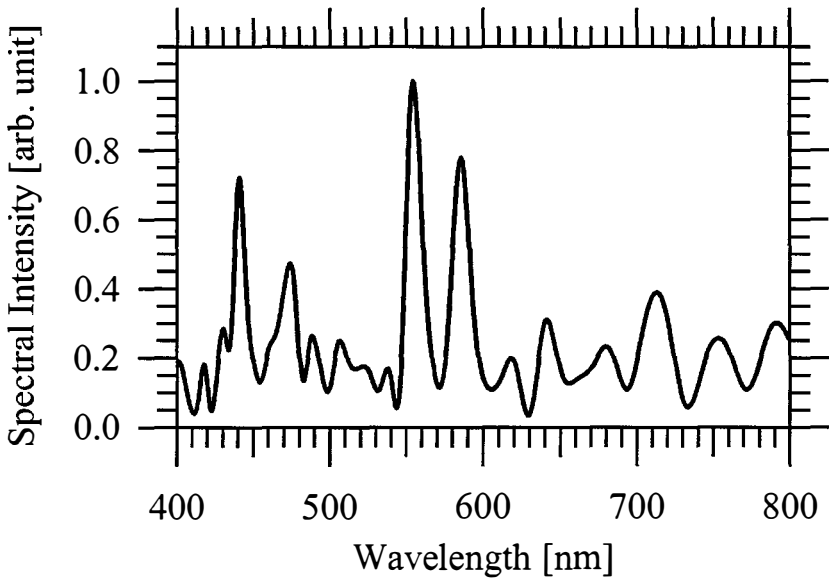

Fig. 4.13 Continuous spectral profile retrieved over the observation plane obtained by taking the Fourier transform of the intensity distribution in Fig. 4.12.

Figure 4.12 shows the intensity distribution of the volume interferogram along the optical path difference, Z, at a particular point in (X, Y) space. Figure 4.13 shows the continuous spectral profile over the observation plane that was obtained by taking the Fourier transform of the intensity distribution in Fig. 4.12. The number of data points is 52, which covers the spectral range from 400 to 800 nm. The spectral resolution is limited by the step interval and number of steps of the PZT. According as the spectral profiles of the MHL and blue LED in Fig. 4.10, we focus on two spectral peaks located at 470.8 and 553.5 nm. The spectral resolutions at these wavelengths are 5.43 and 7.50 nm, respectively.

Figure 4.14(a)–(f) show the complex incoherent hologram at $\lambda = 553.5$ nm and the corresponding reconstructed results for the K mask screen. Figure 4.14(a) shows the phase distribution and Fig. 4.14(b) shows the absolute value of the complex incoherent hologram $W_{12}^{(z_0)}(\rho_\perp;\omega)$. This phase distribution only recorded the wavefront shape of the optical field propagated from the K mask screen because the contribution from the 2 mask screen is small at this spectral component. Figure 4.14(c) shows the phase distribution of the reconstructed image and Fig. 4.14(d) shows the in-focus image over the x-y plane, where the reconstruction distance is $z = 4$ mm. The images of K and 2 are separated clearly. Because the wavefront shape of the 2 mask screen recorded in the phase distribution of the complex incoherent hologram, has been eliminated, this reconstruction distance specifies the in-focus plane of K.

Figures 4.14(e) and (f) show the intensity profiles along the x- and y-directions in the object position of Fig. 4.14(d). From these intensity profiles, the size of the reconstructed object is 0.7×0.8 mm. The shape of the measured object was reconstructed and the size of the letter K was close to the original size of the K in Fig. 4.11(a). Figure 4.15(a) and (b) show the intensity distributions over the x-z and y-z planes and Fig. 4.15(c) shows the intensity profile along the z-direction at $\lambda = 553.5$ nm. The intensity peak is close to $z = 4$ mm, which is in agreement with the object position, $z_1 = 5$ mm.

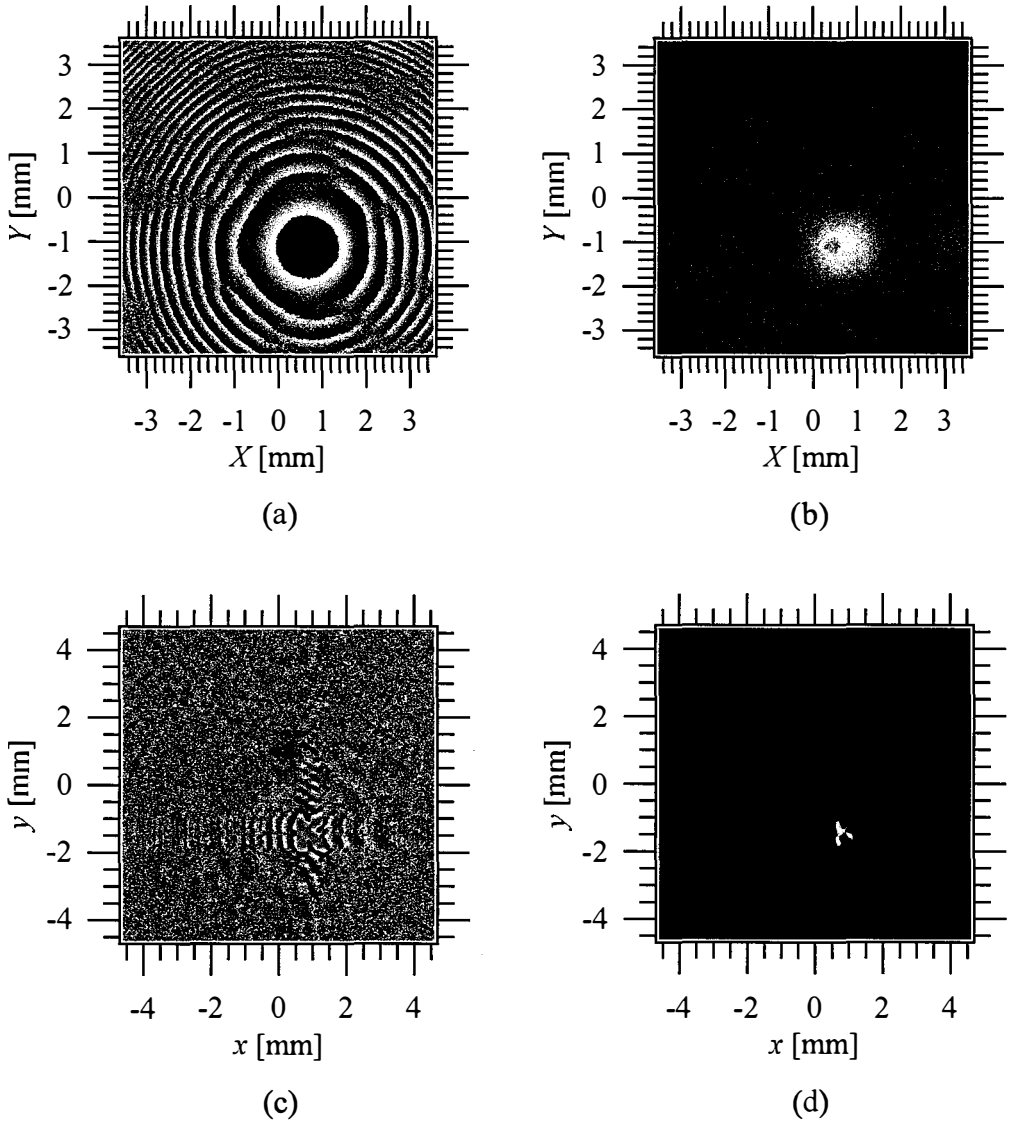

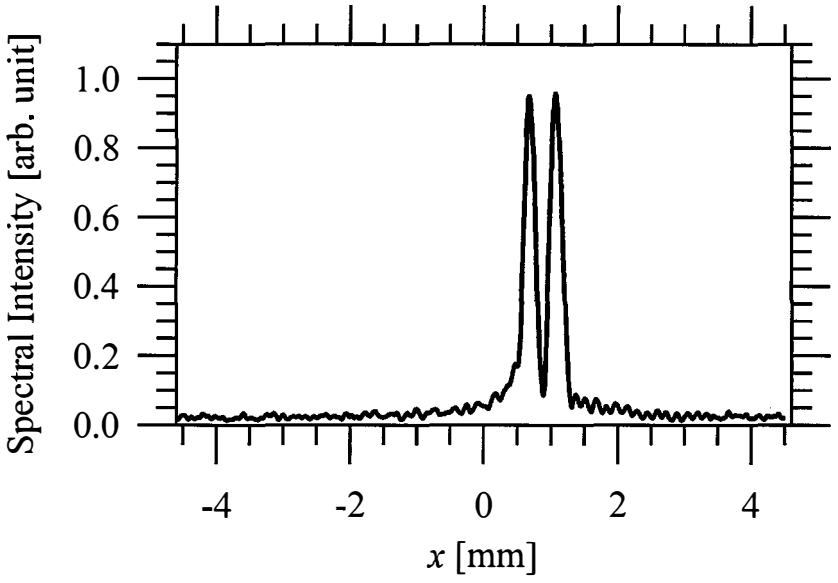

(e)

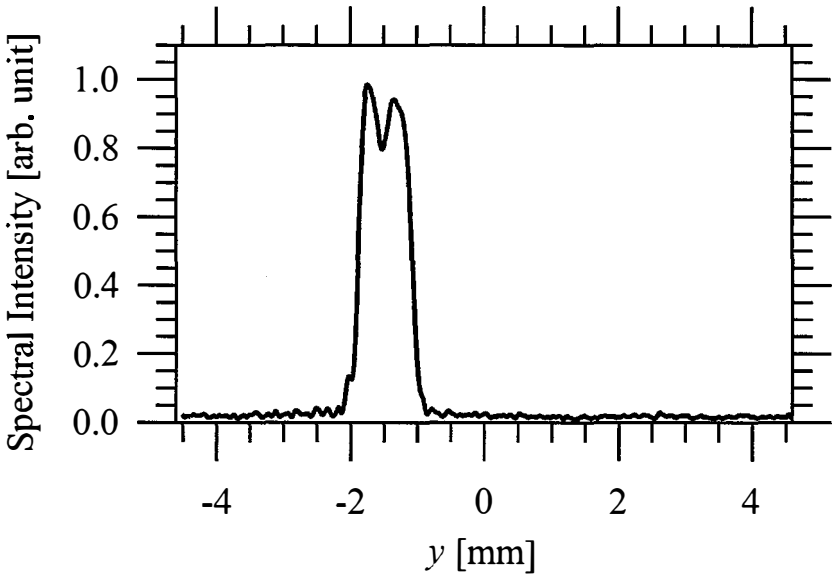

(f)

Fig. 4.14 (a) Phase distribution and (b) absolute value of the complex incoherent hologram at spectral peak $\lambda = 553.5$ nm. (c) Phase distribution of the reconstructed image and (d) in-focus images over the x-y plane at $z = 4$ mm. Intensity profiles along the (e) x- and (f) y-directions at the object position in (d).

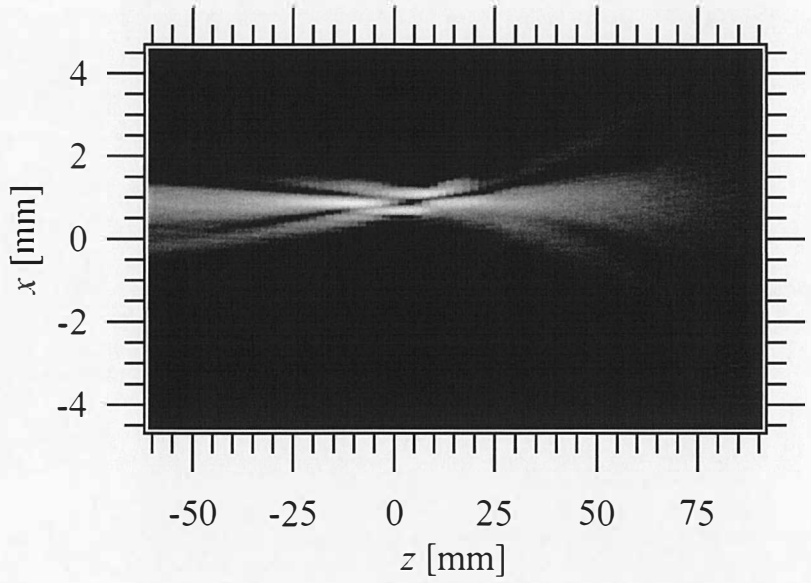

(a)

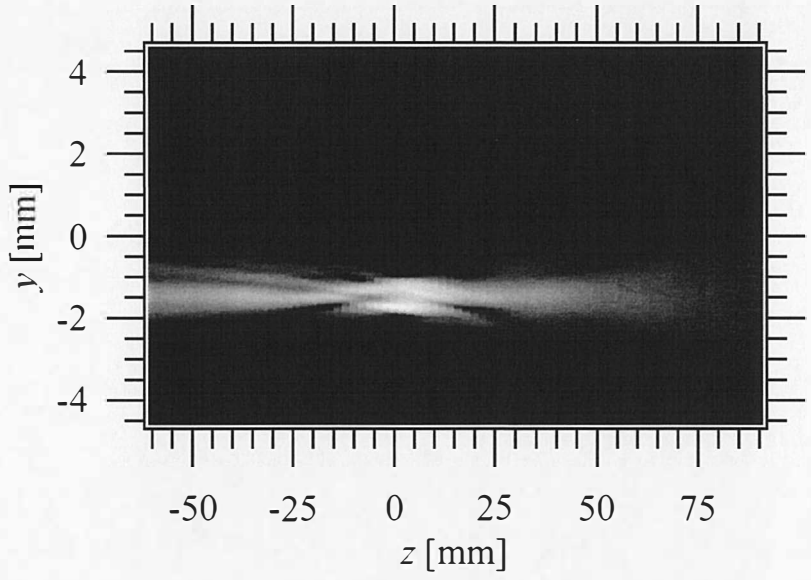

(b)

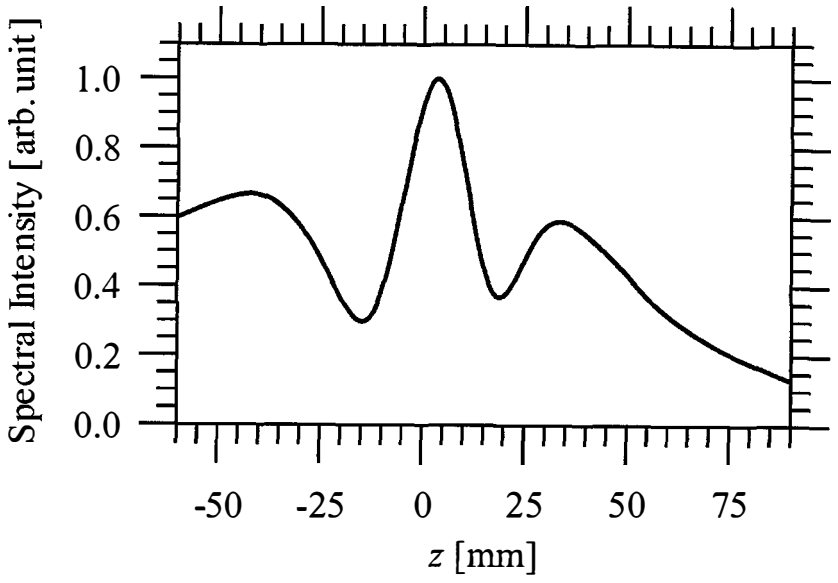

(c)

Fig. 4.15 Intensity distributions of the K mask screen over the (a) x-z and (b) y-z planes. (c) Intensity profile of the reconstructed image along the z-direction at $\lambda = 553.5$ nm.

Similarly, Fig. 4.16(a)–(f) show the complex incoherent hologram at $\lambda = 470.8$ nm and the reconstructed results for the 2 mask screen obtained from the complex incoherent hologram. Figure 4.16(a) shows the phase distribution and Fig. 4.16(b) shows the absolute value of the complex incoherent hologram. Because the two objects have this spectral component, the wavefront shapes of the optical field propagated from both objects are recorded. Figure 4.16(c) shows the phase distribution of the reconstructed image and Fig. 4.16(d) shows the in-focus image, where the reconstruction distance is $z = -6$ mm. From these reconstructed results, the reconstructed images of the 2 and K mask screens were obtained. However, K was obviously blurred and 2 was focused, which means that the depth distance of the two objects can be distinguished. Figure 4.16(e) and (f) show the intensity profiles along the x- and y-directions in the object position of Fig. 4.16(d). From these intensity profiles, the size of the reconstructed object is 0.7 × 0.9 mm. The shape of the measured object was reconstructed. Figures 4.17(a) and (b) show the intensity distributions over the x-z and y-z planes and Fig. 4.17(c) shows the intensity profile along the z-direction at $\lambda = 470.8$ nm. The intensity peak is close to $z = -6$ mm, which is in agreement with object position, $z_2 = -5$ mm.

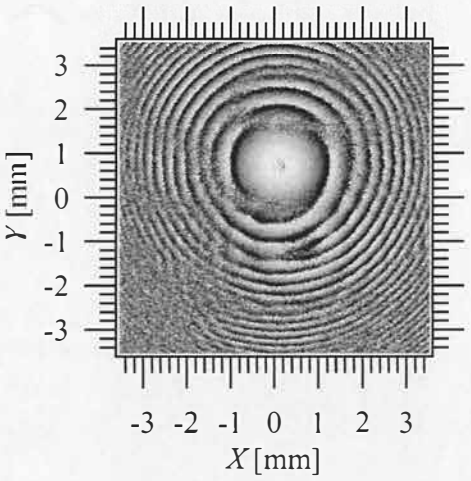
Y [mm]
3
2
1
0
-1
-2
-3
-3 -2 -1 0 1 2 3
X [mm]

(a)

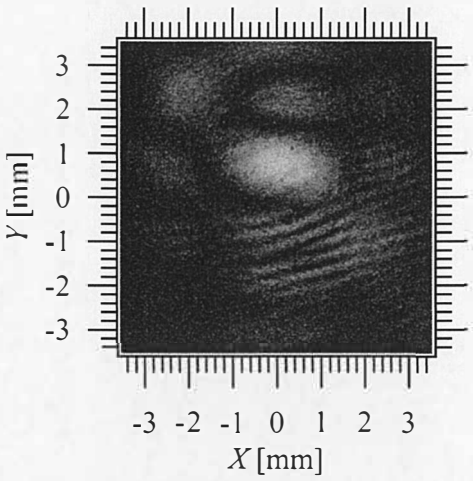
Y [mm]
3
2
1
0
-1
-2
-3
-3 -2 -1 0 1 2 3
X [mm]

(b)

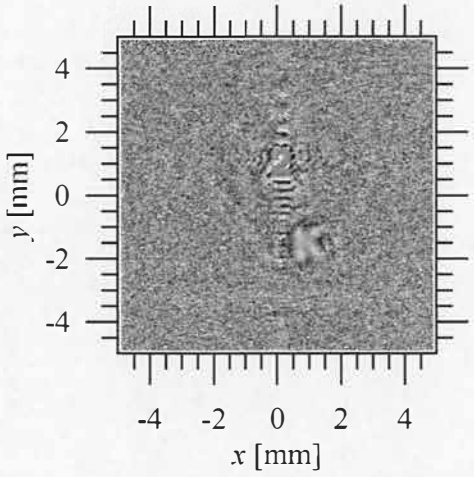
y [mm]
4
2
0
-2
-4
-4 -2 0 2 4
x [mm]

(c)

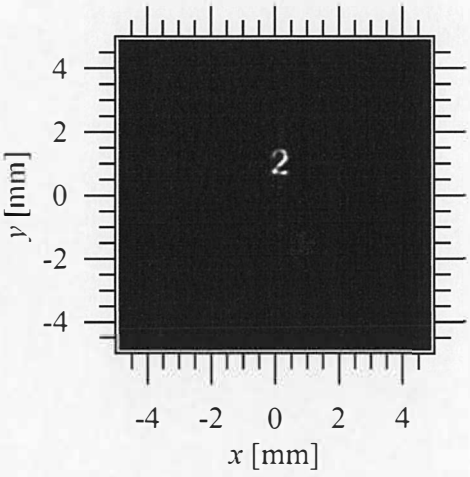
y [mm]
4
2
0
-2
-4
2
-4 -2 0 2 4
x [mm]

(d)

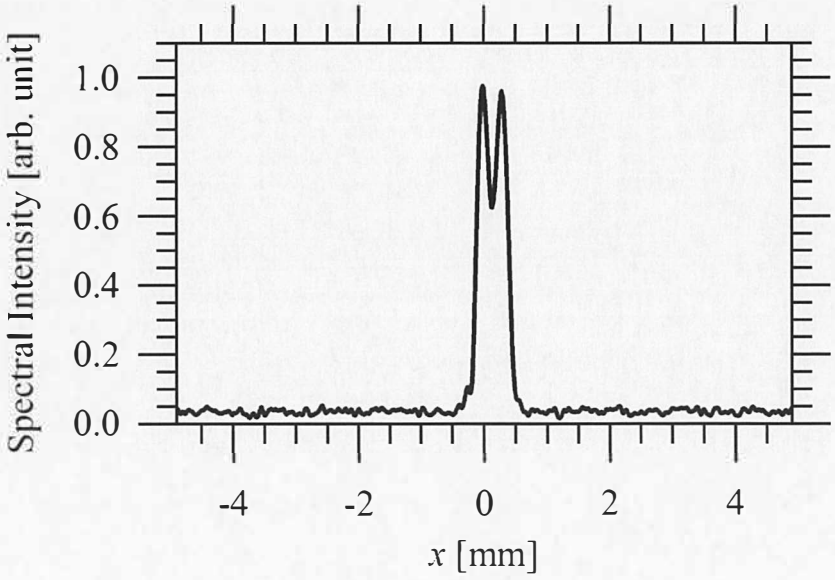
Spectral Intensity [arb. unit]
1.0
0.8
0.6
0.4
0.2
0.0
-4 -2 0 2 4
x [mm]

(e)

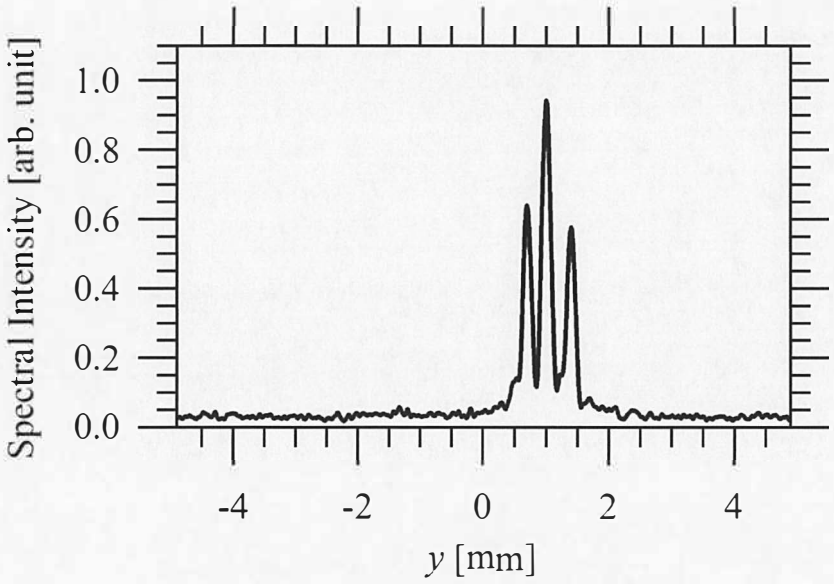

(f)

Fig. 4.16 (a) Phase distribution and (b) absolute value of the complex incoherent hologram at spectral peak $\lambda = 470.8$ nm. (c) Phase distribution of the reconstructed image and (d) in-focus images over the x-y plane at $z = -6$ mm. Intensity profiles along the (e) x- and (f) y-directions at the object position in (d).

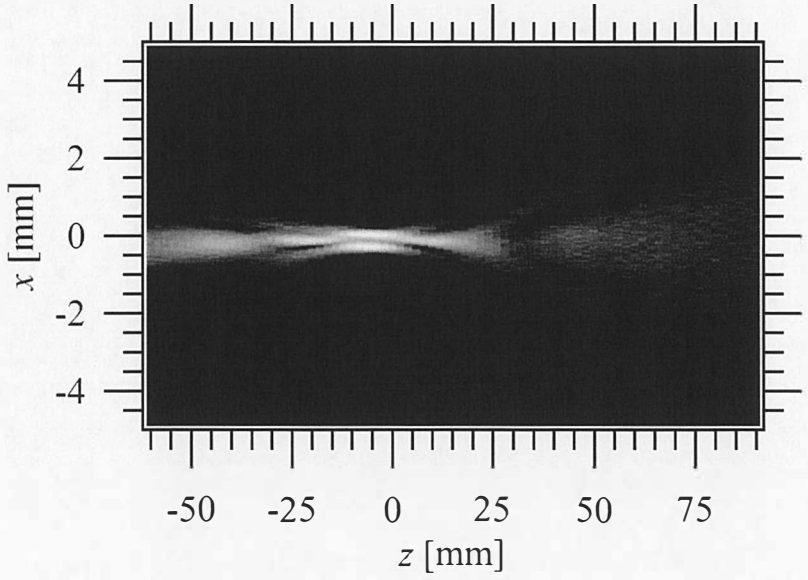

(a)

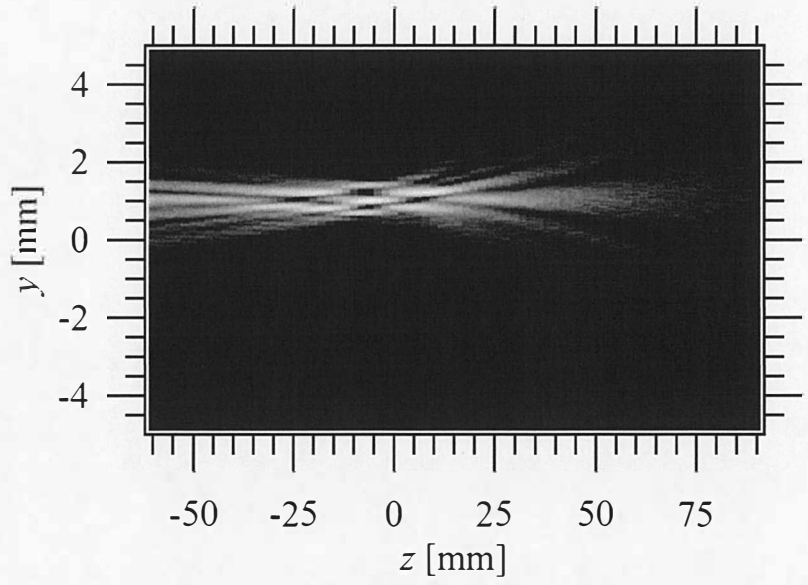

(b)

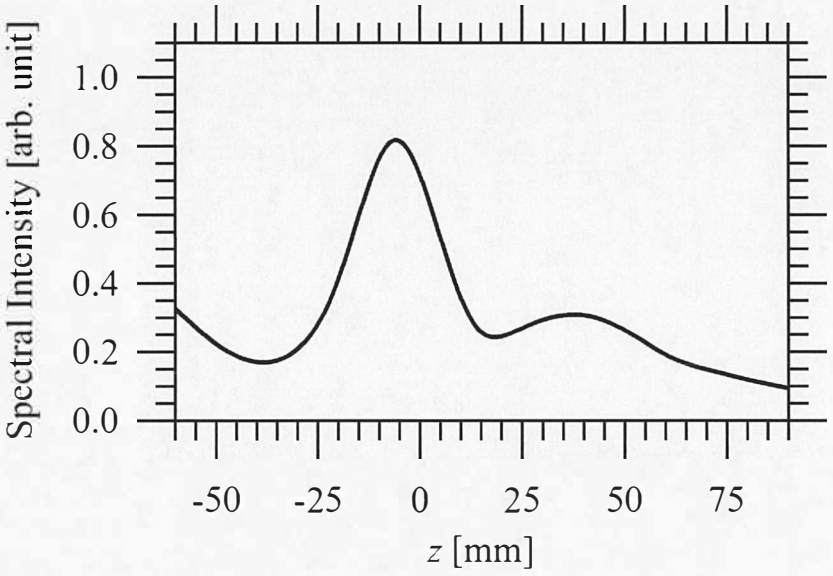

(c)

Fig. 4.17 Intensity distributions of the 2 mask screen over the (a) *x*-*z* and (b) *y*-*z* planes. (c) Intensity profile of the reconstructed image along the *z*-direction at $\lambda = 470.8$ nm.

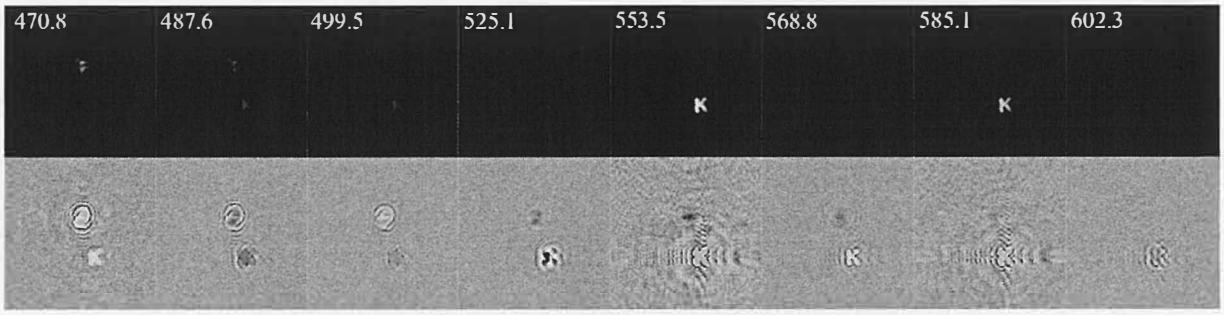

(a)

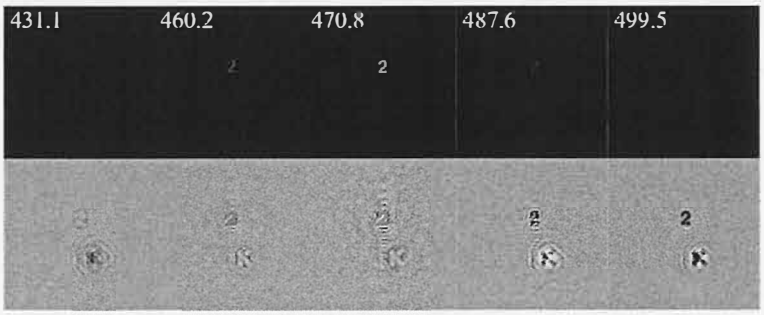

(b)

Fig. 4.18 Reconstructed in-focus spectral images of the object shapes of the K and 2 mask screens for narrow ranges of multiple spectral bands. The in-focus images and the phase distribution are (a) $z = 4$ mm for $\lambda = 470.8 - 602.3$ nm, and (b) $z = -6$ mm for $\lambda = 431.1 - 499.5$ nm.

The measured polychromatic objects in this experiment were the K and 2 mask screens that have different continuous spectra (Fig. 4.10). Figure 4.18(a) and (b) show the reconstructed in-focus spectral images and the phase distributions of K and 2 at different spectral components. The object shapes of the K and 2 mask screens are clearly seen at spectral peaks of 470.8 and 553.5 nm, respectively. Changes in the object intensity and shapes of the K and 2 mask screens are visible at $\lambda = 470.8 - 499.5$ nm because this wavelength range covers the contribution of the spectral components of both the MHL and blue LED, and the positions of the K and 2 mask screens are different. In contrast, only the object shape of the K mask screen is visible at $\lambda = 525.1 - 602.3$ nm because the wavelength range only covers the spectral components of the MHL. These results agree with the combined spectral profile of the MHL and blue LED (Fig. 4.13).

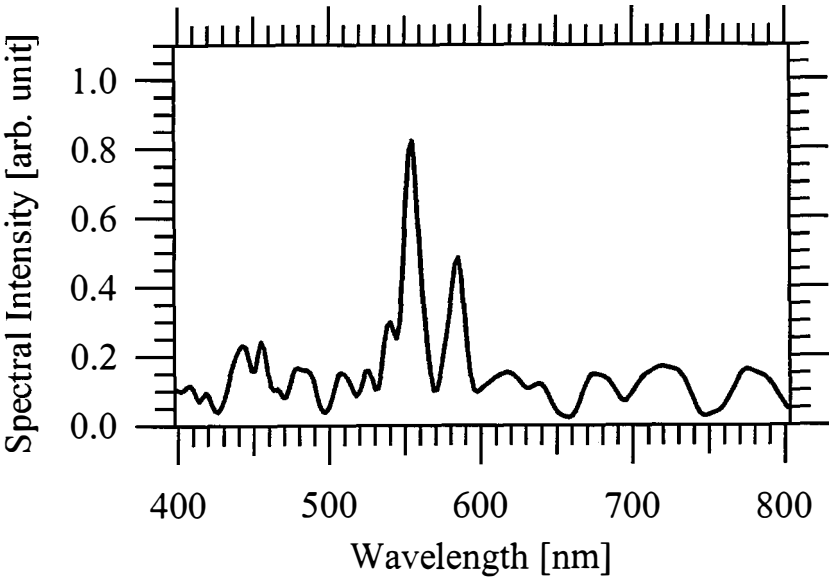

(a)

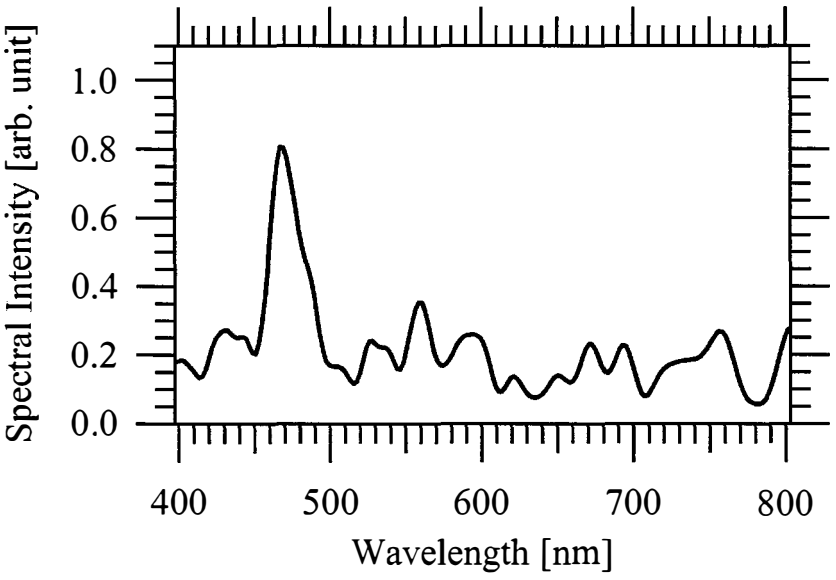

(b)

Fig. 4.19 Separated spectral profiles of the mask screens of the polychromatic objects at the 3D spatial positions on the 3D images of (a) K, $z = 4$ mm and (b) 2, $z = -6$ mm.

Figure 4.19 shows the separated spectral profiles of the in-focus images of the K and 2 at fixed points on the characters. The profiles are obtained by tracking the variation of intensities across the wavelength region, thereby obtaining the continuous spectrum at a specific point on the 3D images. The experimental results agree with the spectral profiles in Fig. 4.10

obtained separately.

Finally, we note that the measurment time of this experiment is 256 seconds for 256 frames. This is about 295 times shorter than our previous work [6] that takes 21 hours, because the present method uses single-axis PZT scan instead of the 3D scan by a single-axis PZT and independent two-axes stages. Measurement time of the previous method is quite long because each stage stops at every sampling point for measuring. In principle, measurement time of the present method may be realized as short as that of Fourier transform spectroscopy.

4.4 Summary

In this chapter, an experimental setup was used to measure mask screens illuminated with incoherent light sources. Based on the interferograms, the volume interferogram was measured directly. By taking the Fourier transform of the volume interferograms with respect to the optical path difference, Z, the spectral profiles of the objects and the complex incoherent hologram for each spectral component were obtained. Subsequently, the 3D image for each spectrum was reconstructed from the complex incoherent hologram by applying the usual inverse propagation techniques. The reconstructed images for each spectrum demonstrated that multispectral images were obtained, validating the method.

V Comparison of imaging properties predicted by the impulse response function and experimental results

5.1 Introduction

This section presents a derivation of the analytical solution of the 4D impulse response function (IRF) of this method. The derivation is performed under the paraxial approximation. For the analytical solution, the measured object is a monochromatic point source represented by a 4D Dirac delta function. For experimental comparison, the measured object is a monochromatic point source with a wavelength of 632.8 nm composed of He-Ne laser light guided by a single-mode optical fiber. To validate the IRF solution, the imaging properties predicted by the IRF are compared with the experimental results.

5.2 Mathematical analysis of 4D IRF of multispectral incoherent holography

This chapter derives an analytical solution of the 4D IRF. Let us first assume that the object to be measured is a monochromatic point source with angular frequency $\omega_s = ck_s = 2\pi c/\lambda_s$, located at position $\boldsymbol{r}_s = (x_s, y_s, z_s)$, and the spatial correlation functions along the x-, y-, and z-axes are measured within baseline lengths of l_x, l_y, and l_z. We may write

$$S_p(\boldsymbol{r};\omega) = \delta^3(\boldsymbol{r} - \boldsymbol{r}_s)\delta(\omega - \omega_s), \tag{5.1}$$

$$A(\boldsymbol{\rho}) = \mathrm{rect}\left(\frac{X}{l_x}\right)\mathrm{rect}\left(\frac{Y}{l_y}\right)\mathrm{rect}\left(\frac{Z}{l_z}\right), \tag{5.2}$$

where $S_p(\boldsymbol{r};\omega)$ is the spectral density of the monochromatic point source located at $\boldsymbol{r}_s$, with unit intensity and the 3D window function, $A(\boldsymbol{\rho})$, assigns the size of the volume interferogram. This window function takes unit value in the measurement area and zero outside. From Eq. (3.7), the measured cross-spectral density function, $W_M^{(z_0)}$, across the

observation plane may be expressed as the Fourier transform of the product of the spatial correlation function in Eq. (3.6) and the window function. Then, the measured cross-spectral density function is expressed as

$$W_M^{(z_0)}(\boldsymbol{\rho}_\perp;\omega_i) = \frac{1}{2\pi c}\int A(\boldsymbol{\rho})\Gamma_{12}(\boldsymbol{\rho})\exp(-ik_iZ)dZ$$
$$= \frac{1}{2\pi}\int_0^\infty A(\boldsymbol{\rho}_\perp)W_{12}^{(z_0)}(\boldsymbol{\rho}_\perp;\omega)\int_{-l_z/2}^{l_z/2}\exp[i(k-k_i)Z]dZdk$$
$$= \frac{l_z}{2\pi c}\int_0^\infty \mathrm{sinc}\left[\frac{l_z}{2c}(\omega-\omega_i)\right]A(\boldsymbol{\rho}_\perp)W_{12}^{(z_0)}(\boldsymbol{\rho}_\perp;\omega)d\omega, \tag{5.3}$$

where $\mathrm{sinc}\,x = (\sin x)/x$. In this equation, subscript i indicates that the parameters are used for the reconstruction, so that the angular frequency for reconstruction is $\omega_i = ck_i = 2\pi c/\lambda_i$. In Eq. (5.3), the product of coefficient $l_z/2\pi c$ and the sinc function represents the spectral IRF that is characterized by the limited baseline length, l_z. Using Eqs. (3.17) and (5.1), we may rewrite Eq. (5.3) as

$$W_M^{(z_0)}(\boldsymbol{\rho}_\perp,\omega_i) = \frac{l_z}{2\pi c}\int_0^\infty \mathrm{sinc}\left[\frac{l_z}{2c}(\omega-\omega_i)\right]A(\boldsymbol{\rho}_\perp)$$
$$\times\kappa\int_\Sigma S_p(\boldsymbol{r};\omega)\exp\left[\frac{ik}{2\gamma(z)}(\boldsymbol{\rho}_\perp - m\boldsymbol{r}_\perp)^2\right]d^3rd\omega$$
$$= \frac{\kappa l_z}{2\pi c}\mathrm{sinc}\left[\frac{l_z}{2c}(\omega_s-\omega_i)\right]A(\boldsymbol{\rho}_\perp)\exp\left[\frac{ik_s}{2\gamma(z_s)}(\boldsymbol{\rho}_\perp - m\boldsymbol{r}_{s\perp})^2\right]. \tag{5.4}$$

In this equation, the measured cross-spectral density function is expressed as a product of the spectral IRF, the 2D aperture function, $A(\boldsymbol{\rho}_\perp) = \mathrm{rect}(X/l_x)\mathrm{rect}(Y/l_y)$, that specifies the size of the complex incoherent hologram, and the quadratic phase factor for the monochromatic point source. From this cross-spectral density function, we reconstruct the 3D image of the monochromatic point source. This image corresponds to the IRF. By applying the inverse propagation formula in Eq. (3.22), the IRF, denoted h, is expressed as

$$h(\boldsymbol{r}_{i\perp}, z_i;\omega_i;\boldsymbol{r}_s,\omega) = \int W_M^{(z_0)}(\boldsymbol{\rho}_\perp,\omega_i)\exp\left[-\frac{ik_i}{2\gamma(z_i)}(\boldsymbol{\rho}_\perp - \boldsymbol{r}_{i\perp})^2\right]d^2\rho_\perp. \tag{5.5}$$

where $d^2\rho_\perp = dXdY$. We define the 3D space vector, $\boldsymbol{r}_i = (x_i, y_i, z_i) = (\boldsymbol{r}_{i\perp}, z_i)$, which specifies the location of the reconstructed image at a reconstruction frequency ω_i. On substituting Eq. (5.4) into Eq. (5.5), we may rewrite the IRF after a straightforward calculation as

$$h(\boldsymbol{r}_i,\omega_i;\,\boldsymbol{r}_s,\,\omega_s)=\frac{\kappa l_z}{2\pi c}\mathrm{sinc}\left[\frac{l_z}{2c}(\omega_s-\omega_i)\right]$$
$$\times\exp\left\{-\frac{ik}{2\gamma(z_i)}\left[(Mm^2x_s^{\,2}-x_i^{\,2})+(Mm^2y_s^{\,2}-y_i^{\,2})\right]\right\}$$
$$\times\int_{-l_x/2}^{l_x/2}\exp\left[-\frac{ik_i}{\gamma(z_i)}\left(Mmx_s-x_i\right)X\right]\exp\left[\frac{ik_i}{2\gamma(z_i)}(M-1)X^2\right]dX$$
$$\times\int_{-l_y/2}^{l_y/2}\exp\left[-\frac{ik_i}{\gamma(z_i)}\left(Mmy_s-y_i\right)Y\right]\exp\left[\frac{ik_i}{2\gamma(z_i)}(M-1)Y^2\right]dY. \tag{5.6}$$

Here, we introduce the degrees of focusing, M, as

$$M=\frac{k_s\gamma(z_i)}{k_i\gamma(z_s)}=\frac{\lambda_i\gamma(z_i)}{\lambda_s\gamma(z_s)}. \tag{5.7}$$

In Eq. (5.7), M is defined as the ratio of the product of wavelength and differential curvature radius of the object and the reconstructed image. Next, let us consider Eq. (5.6), the integral term of which is classified into three cases as follows.

Case 1: Degrees of focusing $M=1$, that is, $\lambda_i\gamma(z_i)=\lambda_s\gamma(z_s)$

In this case, the quadratic phase factors in the integrations by X and Y on the right-hand side of Eq. (5.6) vanish. Thus, after simple calculation, Eq. (5.6) is expressed as

$$h(\boldsymbol{r}_i,\omega_i;\boldsymbol{r}_s,\omega_s)=\frac{\kappa l_x l_y l_z}{2\pi}\exp\left[\frac{ik_i}{2\gamma(z_i)}(m^2\boldsymbol{r}_{s\perp}^{\,2}-\boldsymbol{r}_{i\perp}^{\,2})\right]\mathrm{sinc}\left[\frac{l_z}{2c}(\omega_s-\omega_i)\right]$$
$$\times\mathrm{sinc}\left[\frac{l_x k_i}{2\gamma(z_i)}(mx_s-x_i)\right]\mathrm{sinc}\left[\frac{l_y k_i}{2\gamma(z_i)}(my_s-y_i)\right]. \tag{5.8}$$

Case 2: Degrees of focusing $M\neq 1$, $0<M<1$, that is, $\lambda_i\gamma(z_i)\neq\lambda_s\gamma(z_s)$

In this case, $M-1=-|M-1|$, and the integral term in Eq. (5.6) is transformed into a perfect square expression,

$$h(\boldsymbol{r}_i,\omega_i;\,\boldsymbol{r}_s,\,\omega_s)=\frac{\kappa l_z}{2\pi c}\mathrm{sinc}\left[\frac{l_z}{2c}(\omega_s-\omega_i)\right]$$
$$\times\exp\left\{-\frac{ik}{2\gamma(z_i)}\left[(Mm^2x_s^{\,2}-x_i^{\,2})+(Mm^2y_s^{\,2}-y_i^{\,2})\right]\right\}$$

$$\times \int_{-l_x/2}^{l_x/2} \exp\left\{\frac{ik_i}{2\gamma(z_i)}(M-1)\left[X-\frac{(Mmx_s-x_i)}{M-1}\right]^2\right\}$$

$$\times \exp\left\{-\frac{ik_i}{2\gamma(z_i)}\frac{(Mmx_s-x_i)^2}{M-1}\right\}dX$$

$$\times \int_{-l_y/2}^{l_y/2} \exp\left\{\frac{ik_i}{2\gamma(z_i)}(M-1)\left[Y-\frac{(Mmy_s-y_i)}{M-1}\right]^2\right\}$$

$$\times \exp\left\{-\frac{ik_i}{2\gamma(z_i)}\frac{(Mmy_s-y_i)^2}{M-1}\right\}dY. \tag{5.9}$$

Here, we introduce new parameters τ_x and τ_y that are expressed as

$$\sqrt{\frac{\pi}{2}}\tau_x = \sqrt{\frac{k_i(M-1)}{2\gamma(z_i)}}\left[X-\frac{(Mmx_s-x_i)}{M-1}\right] \tag{5.10}$$

$$\sqrt{\frac{\pi}{2}}\tau_y = \sqrt{\frac{k_i(M-1)}{2\gamma(z_i)}}\left[Y-\frac{(Mmy_s-y_i)}{M-1}\right]. \tag{5.11}$$

Substituting Eqs. (5.10) and (5.11) into Eq. (5.9) yields

$$h(\boldsymbol{r}_i,\omega_i;\boldsymbol{r}_s,\omega_s) = \frac{\kappa l_z}{2\pi c}\operatorname{sinc}\left[\frac{l_z}{2c}(\omega_s-\omega_i)\right]$$

$$\times \exp\left\{-\frac{ik_i}{2\gamma(z_i)}\left[(Mm^2x_s^2-x_i^2)+(Mm^2y_s^2-y_i^2)\right]\right\}$$

$$\times i\sqrt{\frac{\pi\gamma(z_i)}{k_i|M-1|}}\exp\left[\frac{ik_i}{2\gamma(z_i)|M-1|}(Mmx_s-x_i)^2\right]\int_{i\alpha^-}^{i\alpha^+}\exp\left(i\frac{\pi}{2}\tau_x^2\right)d\tau_x$$

$$\times i\sqrt{\frac{\pi\gamma(z_i)}{k_i|M-1|}}\exp\left[\frac{ik_i}{2\gamma(z_i)|M-1|}(Mmy_s-y_i)^2\right]\int_{i\beta^-}^{i\beta^+}\exp\left(i\frac{\pi}{2}\tau_y^2\right)d\tau_y, \tag{5.12}$$

where

$$\alpha^{\pm} = \sqrt{\frac{k_i|M-1|}{\pi\gamma(z_i)}}\left(\pm\frac{l_x}{2}-\frac{Mmx_s-x_i}{M-1}\right), \tag{5.13}$$

$$\beta^{\pm} = \sqrt{\frac{k_i|M-1|}{\pi\gamma(z_i)}}\left(\pm\frac{l_y}{2}-\frac{Mmy_s-y_i}{M-1}\right). \tag{5.14}$$

The integral with respect to τ_x in Eq. (5.12) is represented as an expression of the Fresnel integrals, $\mathbf{C}(a)$ and $\mathbf{S}(a)$, as

$$\int_{i\alpha^-}^{i\alpha^+} \exp\left(i\frac{\pi}{2}\tau_x^{\,2}\right)d\tau_x = \left[\mathbf{C}(i\alpha^+) - i\mathbf{S}(i\alpha^+)\right] - \left[\mathbf{C}(i\alpha^-) - i\mathbf{S}(i\alpha^-)\right]$$

$$= i\sqrt{2}\exp(-i\frac{\pi}{4})\left\{\mathbf{F}^{(*)}(\alpha^+) - \mathbf{F}^{(*)}(\alpha^-)\right\}, \tag{5.15}$$

where the terms indicated by (*) appears only if $0 < M < 1$. The function $\mathbf{F}(a)$[8] is defined as

$$\mathbf{F}(a) = \frac{1}{1+i}\int_{-\infty}^{a} \exp\left(i\frac{\pi}{2}\tau^2\right)d\tau$$

$$= \frac{1}{\sqrt{2}}\exp\left(-i\frac{\pi}{4}\right)\left\{\frac{1}{2} + \mathbf{C}(a) + i\left[\frac{1}{2} + \mathbf{S}(a)\right]\right\}, \tag{5.16}$$

where

$$\mathbf{C}(a) = \int_0^a \cos\left(\frac{\pi}{2}\tau^2\right)d\tau, \tag{5.17}$$

$$\mathbf{S}(a) = \int_0^a \sin\left(\frac{\pi}{2}\tau^2\right)d\tau, \tag{5.18}$$

are the Fresnel integrals.[9] Substituting Eq. (5.15) into Eq. (5.12), and then using a similar procedure for the integral with respect to τ_y, the analytical solution of the cross-spectral density can be written as

$$h(\boldsymbol{r}_i, \omega_i; \boldsymbol{r}_s, \omega_s) = \frac{\kappa l_z \gamma(z_s)}{k_i\,|M-1|}\exp\left(-i\frac{\pi}{2}\right)\mathrm{sinc}\left[\frac{l_z}{2c}(\omega_s - \omega_i)\right]$$

$$\times \exp\left[\frac{ik_i}{2\gamma(z_i)}(Mm^2\boldsymbol{r}_{s\perp}^{\,2} - \boldsymbol{r}_{i\perp}^{\,2})\right]\exp\left[\frac{ik_i}{2\gamma(z_i)\,|M-1|}(Mm\boldsymbol{r}_{s\perp} - \boldsymbol{r}_{i\perp})^2\right]$$

$$\times\left[\mathbf{F}^{(*)}(\alpha^+) - \mathbf{F}^{(*)}(\alpha^-)\right]\left[\mathbf{F}(\beta^+) - \mathbf{F}(\beta^-)\right]. \tag{5.19}$$

Case 3: Degrees of focusing $M \neq 1$, $M > 1$, that is, $\lambda_i\gamma(z_i) \neq \lambda_s\gamma(z_s)$

In this case, $M - 1 = |M - 1|$, Eq. (5.12) is represented as

$$h(\boldsymbol{r}_i,\omega_i;\boldsymbol{r}_s,\omega_s)=\frac{\kappa l_z}{2\pi c}\operatorname{sinc}\left[\frac{l_z}{2c}(\omega_s-\omega_i)\right]$$
$$\times\exp\left\{-\frac{ik_i}{2\gamma(z_i)}\left[(Mm^2x_s^{\,2}-x_i^{\,2})+(Mm^2y_s^{\,2}-y_i^{\,2})\right]\right\}$$
$$\times\sqrt{\frac{\pi\gamma(z_i)}{k_i|M-1|}}\exp\left[-\frac{ik_i}{2\gamma(z_i)|M-1|}(Mmx_s-x_i)^2\right]\int_{i\alpha^-}^{i\alpha^+}\exp\left(i\frac{\pi}{2}\tau_x^{\,2}\right)d\tau_x$$
$$\times\sqrt{\frac{\pi\gamma(z_i)}{k_i|M-1|}}\exp\left[-\frac{ik_i}{2\gamma(z_i)|M-1|}(Mmy_s-y_i)^2\right]\int_{i\beta^-}^{i\beta^+}\exp\left(i\frac{\pi}{2}\tau_y^{\,2}\right)d\tau_y. \tag{5.20}$$

The integral with respect to τ_x in Eq. (5.20) is represented by

$$\int_{i\alpha^-}^{i\alpha^+}\exp\left(i\frac{\pi}{2}\tau_x^{\,2}\right)d\tau_x=\left[\mathbf{C}(i\alpha^+)-i\mathbf{S}(i\alpha^+)\right]-\left[\mathbf{C}(i\alpha^-)-i\mathbf{S}(i\alpha^-)\right]$$
$$=\sqrt{2}\exp(i\frac{\pi}{4})\left\{\mathbf{F}(\alpha^+)-\mathbf{F}(\alpha^-)\right\}. \tag{5.21}$$

Therefore, Eq. (5.20) can be expressed as

$$h(\boldsymbol{r}_i,\omega_i;\boldsymbol{r}_s,\omega_s)=\frac{\kappa l_z\gamma(z_s)}{k_i\,|M-1|}\exp\left(i\frac{\pi}{2}\right)\operatorname{sinc}\left[\frac{l_z}{2c}(\omega_s-\omega_i)\right]$$
$$\times\exp\left[\frac{ik_i}{2\gamma(z_i)}(Mm^2\boldsymbol{r}_{s\perp}^{\,2}-\boldsymbol{r}_{i\perp}^{\,2})\right]\exp\left[-\frac{ik_i}{2\gamma(z_i)\,|M-1|}(Mm\boldsymbol{r}_{s\perp}-\boldsymbol{r}_{i\perp})^2\right]$$
$$\times\left[\mathbf{F}(\alpha^+)-\mathbf{F}(\alpha^-)\right]\left[\mathbf{F}^{(*)}(\beta^+)-\mathbf{F}^{(*)}(\beta^-)\right]. \tag{5.22}$$

Thus, the final expression of the 4D IRF as found by the proposed method is written

$$h(\boldsymbol{r}_i,\omega_i;\boldsymbol{r}_s,\omega_s)=\frac{\kappa l_z\gamma(z_s)}{k_i\,|M-1|}\exp^{(*)}\left(i\frac{\pi}{2}\right)\operatorname{sinc}\left[\frac{l_z}{2c}(\omega_s-\omega_i)\right]$$
$$\times\exp\left[\frac{ik_i}{2\gamma(z_i)}(Mm^2\boldsymbol{r}_{s\perp}^{\,2}-\boldsymbol{r}_{i\perp}^{\,2})\right]$$
$$\times\exp^{(*)}\left[-\frac{ik_i}{2\gamma(z_i)\,|M-1|}(Mm\boldsymbol{r}_{s\perp}-\boldsymbol{r}_{i\perp})^2\right]$$
$$\times\left[\mathbf{F}^{(*)}(\alpha^+)-\mathbf{F}^{(*)}(\alpha^-)\right]\left[\mathbf{F}^{(*)}(\beta^+)-\mathbf{F}^{(*)}(\beta^-)\right], \tag{5.23}$$

5.3 A unified expression of the IRF and system response

From the special cases investigated in the subsection 5.2, 4D IRF may be expressed as in the following unified form:

$$h(\boldsymbol{r}_i,\omega_i;\boldsymbol{r}_s,\omega_s)=\frac{\kappa l_z\gamma(z_i)}{k_i\,|M-1|}\exp^{(*)}\left(i\frac{\pi}{2}\right)\mathrm{sinc}\left[\frac{l_z}{2c}(\omega_s-\omega_i)\right]$$
$$\times\exp\left[\frac{ik_i}{2\gamma(z_i)}(Mm^2\boldsymbol{r}_{s\perp}{}^2-\boldsymbol{r}_{i\perp}{}^2)\right]\exp^{(*)}\left[-\frac{ik_i}{2\gamma(z_i)\,|M-1|}(Mm\boldsymbol{r}_{s\perp}-\boldsymbol{r}_{i\perp})^2\right]$$
$$\times\left[\mathbf{F}^{(*)}(\alpha^+)-\mathbf{F}^{(*)}(\alpha^-)\right]\left[\mathbf{F}^{(*)}(\beta^+)-\mathbf{F}^{(*)}(\beta^-)\right], \tag{5.24}$$

where (*) appear only if $0<M<1$. The function $\mathbf{F}(a)$ is defined by

$$\mathbf{F}(a)=\frac{1}{1+i}\int_{-\infty}^{a}\exp\left(i\frac{\pi}{2}\tau^2\right)d\tau$$
$$=\frac{1}{\sqrt{2}}\exp\left(-i\frac{\pi}{4}\right)\left\{\frac{1}{2}+\mathbf{C}(a)+i\left[\frac{1}{2}+\mathbf{S}(a)\right]\right\}, \tag{5.25}$$

where

$$\mathbf{C}(a)=\int_0^a\cos\left(\frac{\pi}{2}\tau^2\right)d\tau, \tag{5.26}$$

$$\mathbf{S}(a)=\int_0^a\sin\left(\frac{\pi}{2}\tau^2\right)d\tau, \tag{5.27}$$

are the Fresnel integrals.[9] Function $\mathbf{F}(a)$ in Eq. (5.25) represents the complex amplitude of Fresnel diffraction with an infinite linear edge.[8] Arguments α and β of function $\mathbf{F}$ in Eq. (5.24) are expressed as

$$\alpha^{\pm}=\sqrt{\frac{k_i\,|M-1|}{\pi\gamma(z_i)}}\left(\pm\frac{l_x}{2}-\frac{Mmx_s-x_i}{M-1}\right), \tag{5.28}$$

$$\beta^{\pm}=\sqrt{\frac{k_i\,|M-1|}{\pi\gamma(z_i)}}\left(\pm\frac{l_y}{2}-\frac{Mmy_s-y_i}{M-1}\right). \tag{5.29}$$

In Eq. (5.24), if we take the limit of $M\to 1$, this equation reduces to

$$h(\boldsymbol{r}_i,\omega_i;\boldsymbol{r}_s,\omega_s)=\frac{\kappa l_x l_y l_z}{2\pi}\exp\left[\frac{ik_i}{2\gamma(z_i)}(m^2\boldsymbol{r}_{s\perp}{}^2-\boldsymbol{r}_{i\perp}{}^2)\right]\mathrm{sinc}\left[\frac{l_z}{2c}(\omega_s-\omega_i)\right]$$

$$\times\mathrm{sinc}\left[\frac{l_x k_i}{2\gamma(z_i)}(mx_s-x_i)\right]\mathrm{sinc}\left[\frac{l_y k_i}{2\gamma(z_i)}(my_s-y_i)\right]. \tag{5.30}$$

This expression of 4D IRF corresponds to the diffraction-limited in-focus image of the monochromatic point source.

Because the optics and signal processing in our system are linear, the output image, O, is generally expressed as the superposition integral of the input spectral density function and IRF,

$$O(\boldsymbol{r}_i;\omega_i)=\int S(\boldsymbol{r}_s;\omega_s)h(\boldsymbol{r}_i,\omega_i;\boldsymbol{r}_s,\omega)d^3r_s d\omega_s. \tag{5.31}$$

5.4 Comparison of properties predicted by IRF and obtained by experiment

This chapter compares the 4D IRF in Eq. (5.23) and the experimental results. The measured object is a monochromatic point source with a wavelength of 632.8 nm composed of He-Ne laser light guided by a single-mode optical fiber. This monochromatic point source is set close to the origin of the Cartesian coordinate system. Thus, the 3D image obtained experimentally can be compared directly with the 3D point spread function. All the experimental parameters are shown in Table 5.1. The conditions assumed in the numerical calculation by the 4D IRF are the same as the experimental conditions.

The experimental spectral profile is shown in Fig. 5.1. The spectral peak appears near 640 nm, and the spectral resolution is limited by the first zero point of sinc function on the right-hand side of Eq. (5.23). The spectral resolution is $\Delta f = 1/l_z = 244.14\ \mathrm{cm}^{-1}$, where $f = k/2\pi = 1/\lambda$ is the wavenumber. In the wavelength region, the spectral resolution is written as

$$\Delta\lambda = \frac{\lambda^2}{l_z}. \tag{5.25}$$

For $\lambda = 640$ nm, we find $\Delta\lambda = 9.77$ nm. This value agrees with the intervals of spectral channels around the peak, as shown circles in Fig 5.1. These expressions of spectral resolution are common in the field of Fourier transform spectrometry.

Table 5.1. System settings for comparing the imaging properties predicted by the IRF and obtained experimentally.

Parameter		
	d_0	375 mm
	d_1	120 mm
	f_1	524 mm
	z_s	0 mm
PZT	Number of steps	256
	Step interval	80 nm
D	Number of pixels	1024 square
	Pixel size	6.9 μm

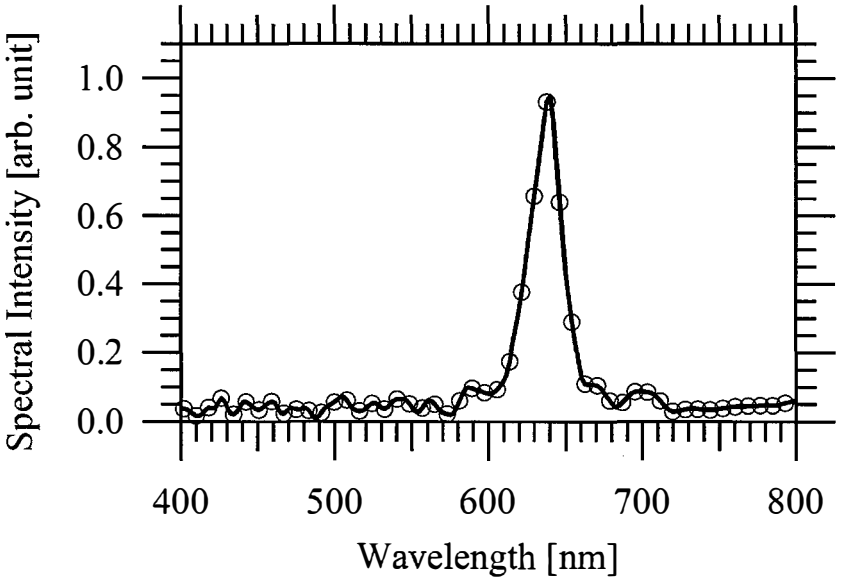

Fig. 5.1. Spectral profile retrieved over the observation plane. Circles indicate data obtained by taking the Fourier transform of the intensity distribution at the center of the volume interferogram with respect to the optical path difference, Z.

The phase distributions of the complex incoherent holograms at the spectral peak calculated using Eq. (5.4) and obtained experimentally agree well (Fig. 5.2(a) and (b)). Figures 5.3–5.5

compare the reconstructed results from the 4D IRF and the experimental results. The in-focus image over the $x_i - y_i$ plane at $z_i = 0$ mm calculated from an analytical solution of the 4D IRF in Eq. (5.23) (Fig. 5.3(a)) and the corresponding image reconstructed from the complex incoherent hologram whose phase distribution is shown in Fig. 5.2(b) (Fig. 5.3(b)) agree well. These images are enlarged for detailed comparison. Figure 5.4 shows the intensity profiles along the *x*-axis in Fig. 5.3; the solid curve shows the experimental results and the dotted curve shows the theoretical results based on the 4D IRF. Figures 5.3 and 5.4 correspond to the intensity profile of a diffraction-limited image of a point source. The experimental and theoretical results both show that for a hologram with a rectangular aperture, the 2D point spread function is represented by the second and third sinc functions of the IRF in Eq. (5.8). Figure 5.5(a) shows the intensity distribution over the $x_i - z_i$ plane calculated from an analytical solution of the 4D IRF and Fig. 5.5(b) shows the corresponding image obtained from the experimental complex incoherent hologram (Fig. 5.2(b)). Figure 5.6 compares the experimental intensity profile (solid curve) with the analytical solution of the 4D IRF (dotted curve) along the *z*-axis across the object position of Fig. 5.5. The peak positions and the distribution shapes agree well. We conclude from these results that the 4D IRF specifies the spectral resolution and 3D imaging properties in multispectral incoherent holography.

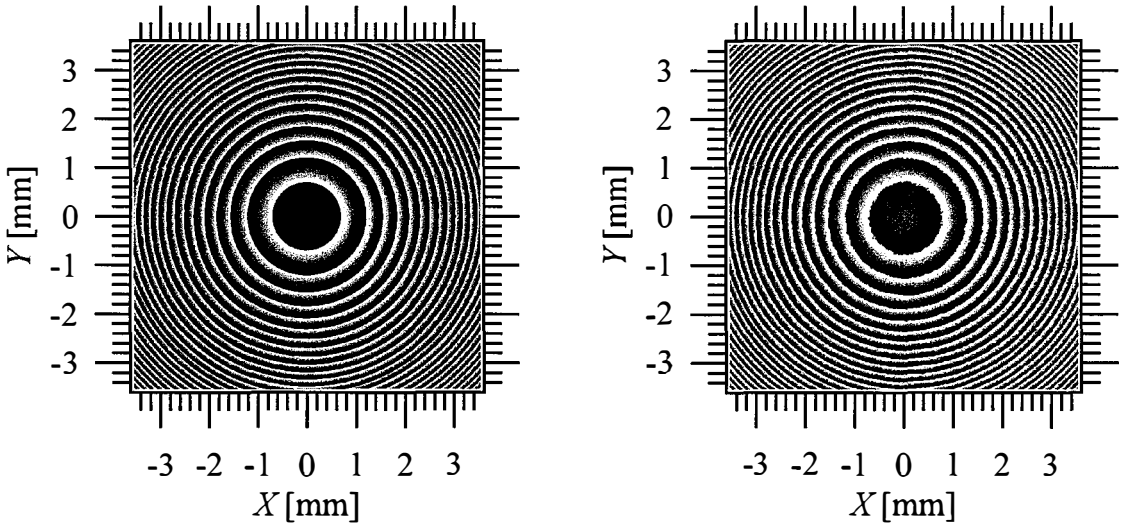

Fig. 5.2. (a) Theoretical and (b) experimental phase distributions of the complex incoherent holograms.

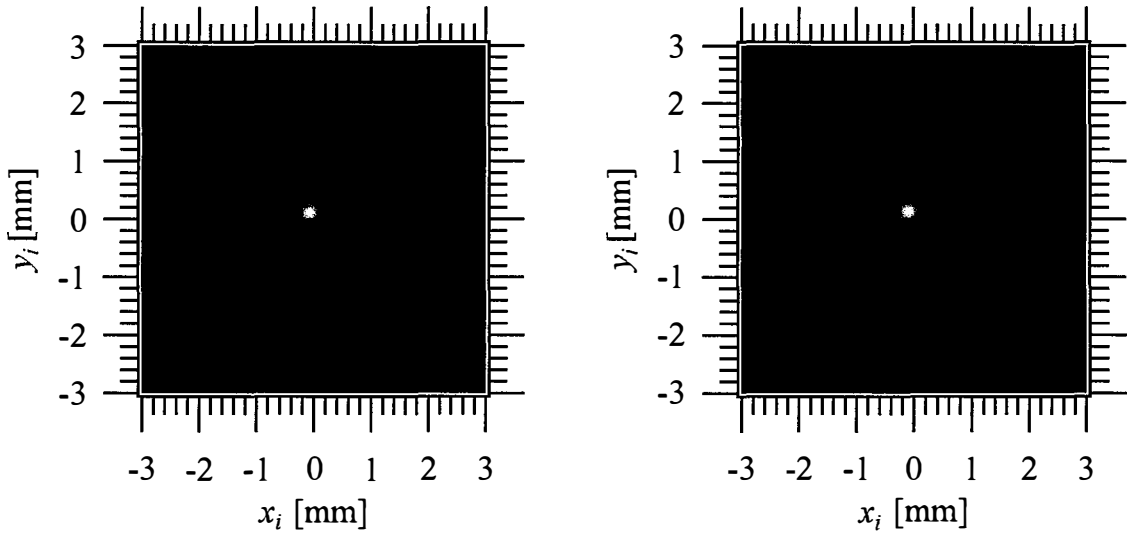

Fig. 5.3. In-focus images over the $x_i - y_i$ plane at λ of 640 nm and a reconstruction distance of $z_i = 0$ mm from (a) the analytical solution of the 4D IRF in Eq. (5.30) and (b) the experimental phase distribution of the complex incoherent hologram shown in Fig. 5.2(b).

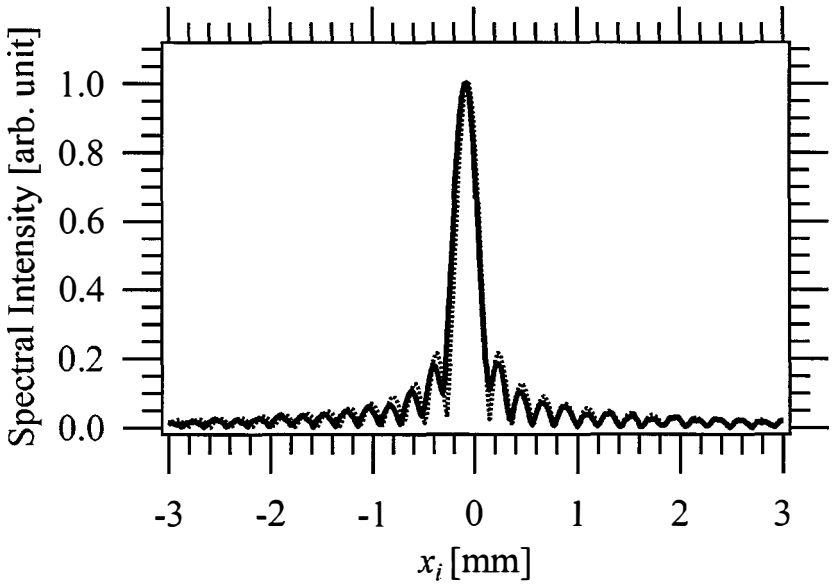

Fig. 5.4. Comparison of the intensity profiles obtained experimentally (solid curve) and from the analytical solution of the 4D IRF in Eq. (5.30) (dotted curve) along the x_i axis.

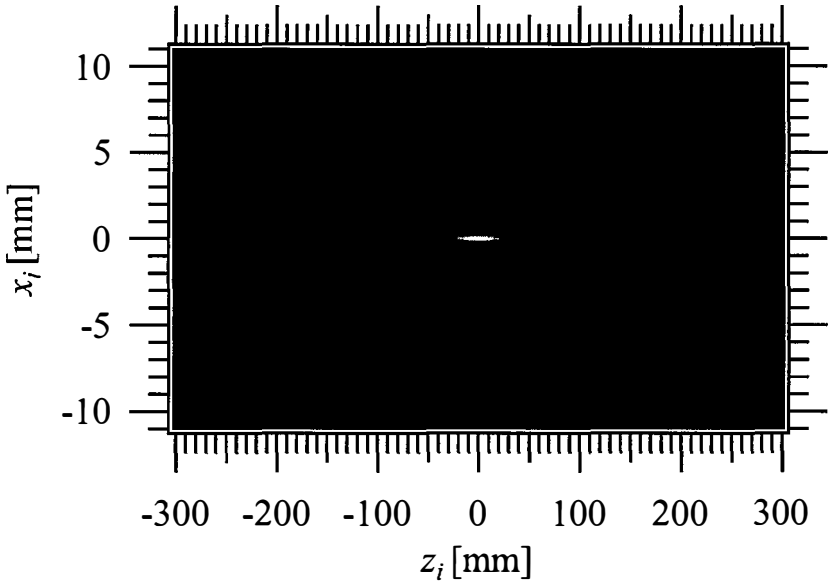

(a)

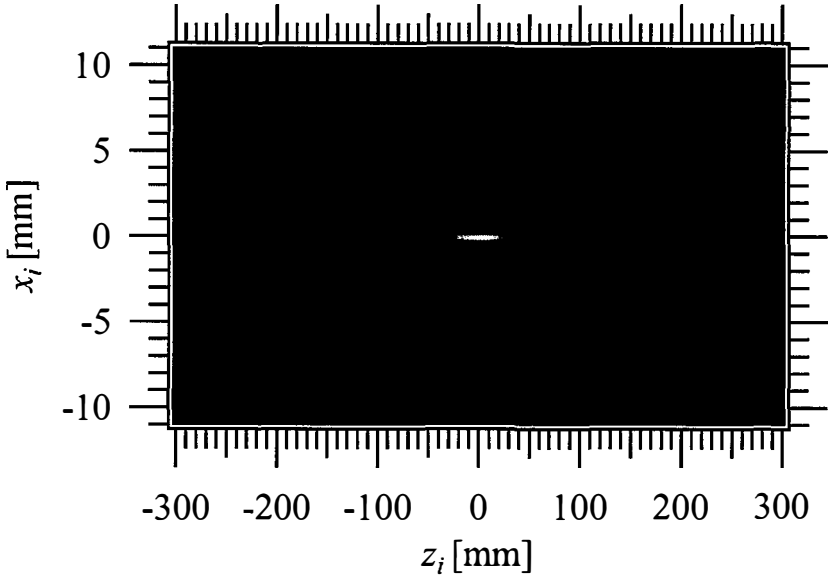

(b)

Fig. 5.5. Intensity profiles along the $x_i - z_i$ plane from the (a) analytical solution of the 4D IRF in Eq. (5.24) and (b) the experimental complex incoherent hologram shown in Fig. 5.2(b).

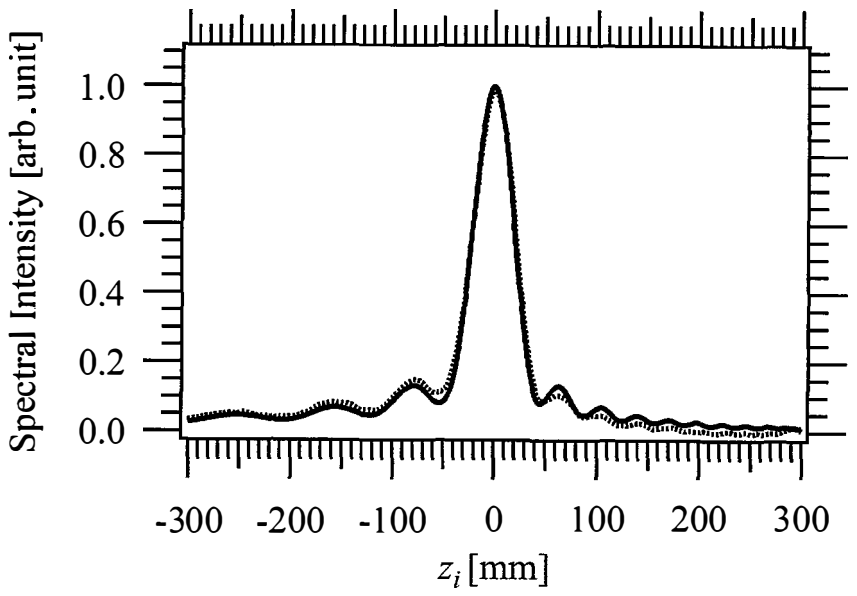

Fig. 5.6. Comparison of intensity profiles obtained experimentally (solid curve) and from the analytical solution of the 4D IRF in Eq. (5.24) (dotted curve) along the z_i axis.

5.5 Summary

The spectral resolution and 3D imaging properties observed experimentally agreed well with the theoretical prediction of the 4D IRF. Thus, these results demonstrate that the 4D IRF can be used to specify the spectral resolution and 3D imaging properties in multispectral incoherent holography.

VI Conclusions

Multispectral incoherent holography, which is based on measuring differential wavefront curvature, was investigated theoretically and experimentally. In this method, a volume interferogram is measured directly by an appropriately designed interferometer. The experimental results showed that 3D spatial information at every spectral component of the measured object was acquired properly with the method. A paraxial IRF defined over the space-frequency domain was derived. Based on this IRF solution, the imaging properties of multispectral incoherent holography were investigated. The spectral resolution and 3D imaging properties observed experimentally agreed well with the theoretical predictions of the 4D IRF. The measurement time of the present method was considerably smaller than those of our previous methods. This simplified lensless optical system is expected to be useful in a wide range of applications, such as biological observation, to provide spectrally resolved 3D images.

Acknowledgements

Throughout the writing of this dissertation, I have received a great deal of support and assistance. I would first like to thank my supervisor, Assoc. Prof. Kyu Yoshimori, whose expertise was invaluable in formulating the research topic and methodology.

I would also like to thank Assist. Prof. Sarai Lekchaum and Assist. Prof. Kitsakorn Locharoenrat who provided me with the opportunity to meet my supervisor. Without their invaluable support, it would not have been possible for me to study abroad in Japan.

I would like to express my gratitude to my lab mates for their feedback, cooperation, and of course their friendship during our time working together, and for all the activities we have shared together over the last three years. In particular, I would like to thank Dr. Masaki Obara for enlightening me and understanding me from my first research experiences. Last but not the least, I would like to thank my parents and brothers for supporting me spiritually throughout the writing of this dissertation and throughout my life.

References

1) K. Yoshimori, "Interferometric spectral imaging for three-dimensional objects illuminated by a natural light source," J. Opt. Soc. Am. A. **18** (2001) 765.
2) M. Sasamoto and K. Yoshimori, "Three-dimensional imaging spectrometry by fully passive interferometry," Opt. Rev. **19** (2012) 29.
3) S. Teeranutranont and K. Yoshimori, "Digital holographic three-dimensional imaging spectrometry," Appl. Opt. **52** (2013) A388.
4) T. Hashimoto, A. Hirai, and K. Yoshimori, "Fully interferometric three-dimensional imaging spectrometry using hyperbolic-type volume interferogram," Appl. Opt. **52** (2013) 1497.
5) M. Obara and K. Yoshimori, "Coherence Three-Dimensional Imaging Spectrometry Based on Measurement of Rotated-Hyperbolic Volume Interferograms," Opt. Rev. **21** (2014) 479.
6) K. Srinuanjan, M. Obara and K. Yoshimori, "Multispectral hyperbolic incoherent holography," Opt. Rev. **25** (2018) 65.
7) J. Rosen, B. Katz, and G. Brooker, "FINCE: Fresnel incoherent correlation hologram, Holography, Research and technologies," In: Prof. J. Rosen (Ed.) InTech (2011) 135.
8) K. Yoshimori, A. Hirai, T. Inoue, K. Itoh, and Y. Ichioka, "Effects of a linear edge on optical imaging" J. Opt. Soc. Am. A **12** (1995) 981.
9) *Handbook of Mathematical Functions with Formulas, Graphs, and Mathematic Tables*, ed. M. Abramowitz and I. Stegun (Dover Publications, Inc., New York, 1970), 9th ed., p. 300.
10) M. Obara and K. Yoshimori, "3D spatial resolution and spectral resolution of interferometric 3D imaging spectrometry," Appl. Opt. **55** (2016) 2489.
11) X. Yu, J. Hong, C. Liu, and M.K. Kim, "Review of digital holographic microscopy for three-dimensional profiling and tracking," Opt. Engineering. **53** (2014) 112306-1.
12) W. Osten, A. Faridian, P. Gao, K. Körner, D. Naik, G. Pedrini, A.K. Singh, M. Takeda, and M. Wilke, "Recent advances in digital holography [Invited]," Appl. Opt. **53** (2014) G44.
13) J. Liu, T. Tahara, Y. Hayasaki, and T. Poon, "Incoherent digital holography: A review," Appl. Sci. **8** (2018) 1.
14) J. Rosen and G. Brooker, "Digital spatially incoherent Fresnel holography," Opt. Lett. **32** (2007) 912.
15) G. Brooker, N. Siegel, V. Wang, and J. Rosen, "Optimal resolution in Fresnel incoherent correlation holographic fluorescence microscopy," Opt. Express **19** (2011) 5047.

16) K.M. Kim, "Full color natural light holographic camera," Opt. Express **21** (2013) 9636.
17) D. N. Naik, G. Pedrini, M. Takeda, and W. Osten, "Spectrally resolved incoherent holography: 3D spatial and spectral imaging using a Mach-Zehnder radial-shearing interferometer," Opt. Lett. **39** (2014) 1857.
18) K. Watanabe and T. Nomura, "Recording spatially incoherent Fourier hologram using dual channel rotational shearing interferometer," Appl. Opt. **54** (2015) A18.
19) J. W. Goodman: *Introduction to Fourier Optics* (McGraw-Hill, New York, 1996) 2nd ed., p. 369.

Relevant original papers and proceedings of international conferences

1. Published paper

1) K. Jianwattananukul, M. Obara, and K. Yoshimori, "Multispectral incoherent holography based on measurement of differential wavefront curvature," Opt. Rev. **xx**, xx-xx (2019).

2. Proceedings of international conferences

1) K. Jianwattananukul, and K. Yoshimori, "Multispectral three-dimensional imaging for the white-light source by measurement of differential wavefront curvature," Proceeding of International symposium on optical memory 2018 (ISOM18), Kitakyushu, Japan, 21-24 October, 33-34, (2018).